Language Modeling with Hyperspherical Flows

Anonymous authors
Paper under double-blind review

Abstract

Discrete Diffusion Language Models progressed rapidly as an alternative to autoregressive (AR) models, motivated by their parallel generation abilities. However, for tractability, discrete diffusion models sample from a factorized distribution, which is less expressive than AR. Recent Flow Language Models (FLMs) apply continuous flows to language, transporting noise to data with a deterministic ODE that avoids factorized sampling. FLMs operate on one-hot vectors whose dimension scales with the vocabulary size, making FLMs costly to train. Moreover, since all distinct one-hot embeddings are equidistant in ℓ_2, adding Gaussian noise does not have a clear semantic interpretation (unlike images, where Gaussian noise progressively degrades structure). We introduce $\mathbb{S}$-FLM, a latent FLM in the hypersphere. $\mathbb{S}$-FLM generates sequences by rotating vectors in $\mathbb{S}^{d-1}$ along a velocity field learned with cross-entropy, avoiding the overhead of materializing one-hot vectors. Previous FLMs match AR in Generative Perplexity (Gen. PPL), but samples with high likelihood are not necessarily correct in verifiable domains such as math and code. $\mathbb{S}$-FLM substantially improves continuous flow language models on large-vocabulary reasoning and closes the gap to masked diffusion under standard-temperature sampling ($T = 1$), while a gap remains under optimized low-temperature ($T = 0.1$) decoding.

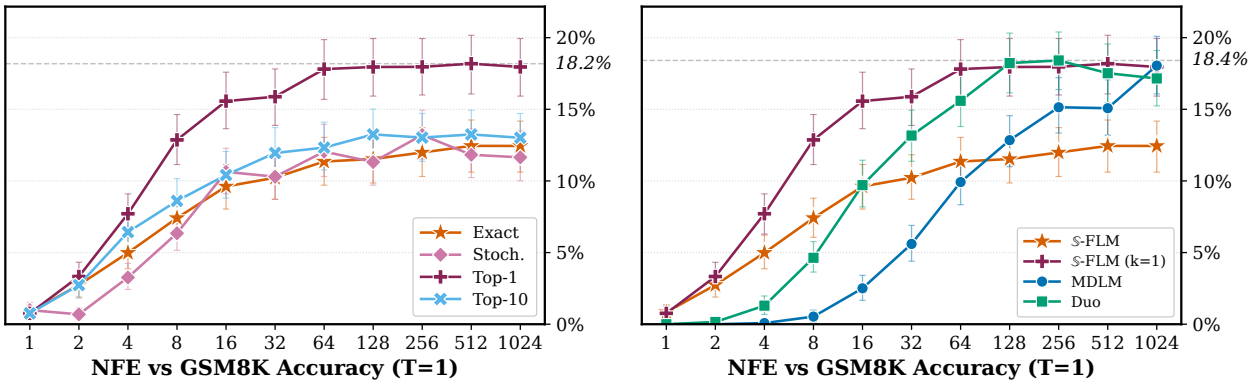

Figure 1: **Accuracy on GSM8K** at $T = 1$. **Left:** Decoding strategies for $\mathbb{S}$-FLM with the $\mathbb{S}$-arch (Sec. 3.3). Exact velocity (15) and stochastic decoding (Algo. 3, *Stoch.*) plateau near 12%. Restricting the velocity to the top-k entries of $p^{\theta}_{1|t}$ improves the accuracy, with top-1 reaching $\sim 18\%$. **Right:** $\mathbb{S}$-FLM (with the $\mathbb{S}$-arch) vs. MDLM and Duo. With the exact velocity, $\mathbb{S}$-FLM beats both baselines at NFE ≤ 16.

1 Introduction

Autoregressive (AR) models currently dominate language modeling. Thanks to the chain-rule factorization and the Transformer architecture (Vaswani et al., 2023), the AR likelihood is fast to evaluate, and AR language models scale to large sizes (Kaplan et al., 2020; OpenAI, 2024a;b; Meta, 2024; Gemini Team et al., 2025; Google, 2025). However, during sampling, AR models need one forward pass per token, and causal

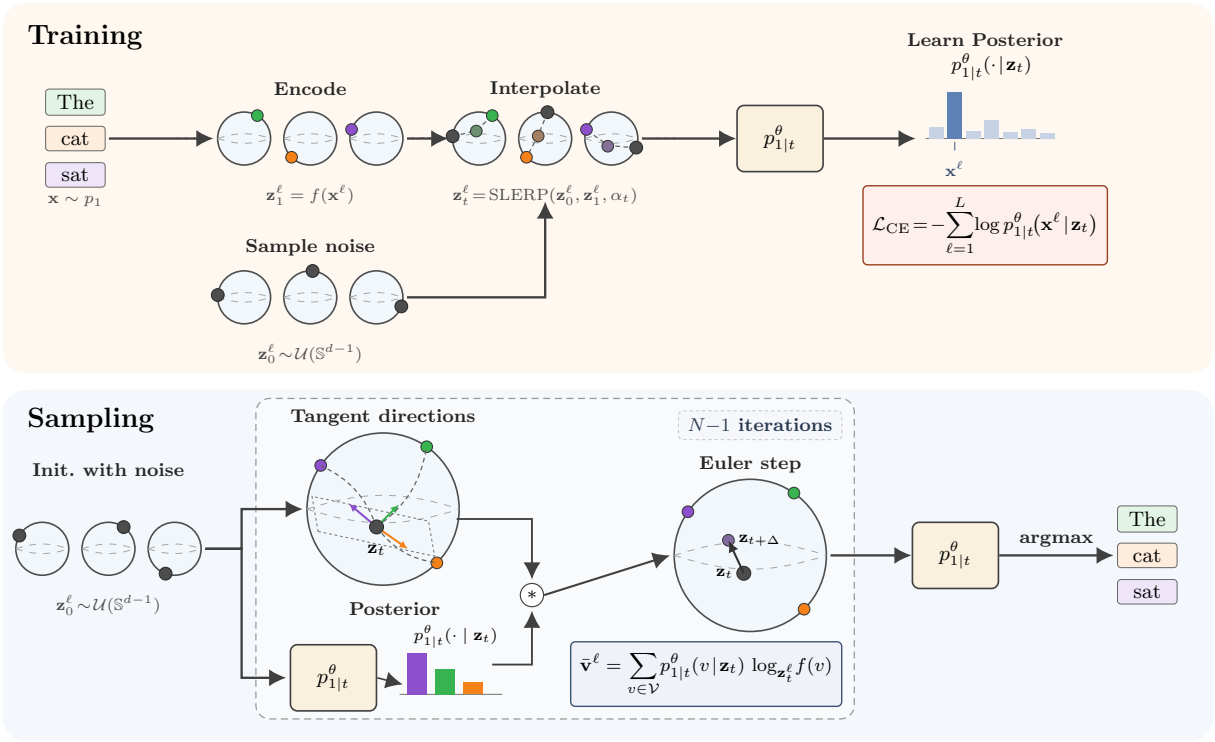

Figure 2: **$\mathbb{S}$-FLM overview. Training (top):** we embed each token as a unit-norm vector on $\mathbb{S}^{d-1}$. We obtain the noisy latent $\mathbf{z}_t^\ell$ by SLERP between the clean embedding and a random vector on $\mathbb{S}^{d-1}$. We train the denoiser $p^\theta_{1|t}$ with cross-entropy. **Sampling (bottom):** $p^\theta_{1|t}$ defines a velocity field by marginalizing over tangent vectors pointing toward each clean embedding $\hat{\mathbf{e}}_v$, $v \in \mathcal{V}$. Starting from uniform noise on $\mathbb{S}^{d-1}$, we integrate along the velocity field and decode the final latent via $\arg\max_{v \in \mathcal{V}} p^\theta_{1|1}(v \mid \mathbf{z}_1)$.

attention can hurt on reasoning tasks, where bidirectional context is required (Papadopoulos et al., 2024; Kitouni et al., 2024; Zhang-Li et al., 2024; Nagarajan et al., 2025).

Discrete diffusion models (Austin et al., 2023; Campbell et al., 2022; Sahoo et al., 2024; Gat et al., 2024; Sahoo et al., 2025a; Shi et al., 2025; Nie et al., 2025; von Rütte et al., 2026; Sahoo et al., 2026; Wu et al., 2025) approach AR models in Generative Perplexity (Gen. PPL), with parallel generation and bidirectional context. However, at each denoising step, tokens are *sampled* from factorized marginals rather than jointly. The factorization makes discrete diffusion less expressive than AR models when generating tokens in parallel.

Continuous flows trained with Flow Matching (Lipman et al., 2023; Liu et al., 2022; Albergo & Vanden-Eijnden, 2023) learn a velocity field that defines an *Ordinary Differential Equation* (ODE), transporting noisy samples to the data distribution. Thus, inference steps update all positions jointly and avoid the factorized sampling issue of discrete diffusion.

Recent work (Roos et al., 2026; Lee et al., 2026; Potaptchik et al., 2026) revived the interest in flow-based language models (Li et al., 2022; Dieleman et al., 2022; Gulrajani & Hashimoto, 2023), known as *Flow Language Models* (FLMs). Recent FLMs represent tokens as one-hot vectors, add Gaussian noise, and train a denoiser with Cross-Entropy (CE). Although they match the Gen. PPL of AR and discrete diffusion models, these FLMs have two main shortcomings. **(1)** Firstly, representing tokens as one-hot vectors is costly. *Large Language Models* (LLMs) commonly use vocabularies containing 100k–200k tokens (OpenAI, 2024b; Qwen Team, 2025), thus large FLMs would need to store a $>$ 100k-dimensional vector for every token. After adding Gaussian noise to these one-hot vectors, the denoiser multiplies them with the embedding matrix instead of looking up a single vector. Therefore, FLMs are slower to train than discrete diffusion and AR models. **(2)**

Secondly, in images, Gaussian diffusion smoothly degrades higher-frequency components first. For one-hot vectors, the interpretation of adding Gaussian noise is not as clear.

Contributions We propose the *Hyperspherical Flow Language Model* ($\mathbb{S}$-FLM), a flow over embeddings that does not need to materialize one-hot vectors. **(1)** Recall that the cosine distance captures the similarity between token embeddings better than the Euclidean distance (Mikolov et al., 2013; Pennington et al., 2014; Wang & Isola, 2020). Since the cosine distance is determined by the arc length on the unit hypersphere, we implement $\mathbb{S}$-FLM as a Riemannian flow on $\mathbb{S}^{d-1}$. Our forward process transports unit-norm embeddings toward a uniform prior. **(2)** $\mathbb{S}$-FLM operates on d-dimensional embeddings rather than $|\mathcal{V}|$-dimensional one-hot vectors. Thus, assuming the same backbone, $\mathbb{S}$-FLM has a similar training cost as discrete diffusion models (unlike FLMs over one-hot vectors, which are costlier). We further introduce the $\mathbb{S}$-arch, a backbone whose activations lie on $\mathbb{S}^{d-1}$. Aligning the activations with the input improves the sample quality on GSM8K and OpenWebText (OWT) (Gokaslan & Cohen, 2019). **(3)** On GSM8K, the accuracy of prior FLMs trained on TinyGSM (Liu et al., 2023) is less than 1%. In contrast, $\mathbb{S}$-FLM reaches $\sim 12\%$ with the exact velocity and $\sim 18\%$ with the top-1 velocity (Sec. 3.1). At standard-temperature sampling ($T = 1$), $\mathbb{S}$-FLM closes the gap to MDLM and Duo with the top-1 velocity across *Number of Function Evaluations* (NFE) budgets, and outperforms them with the exact velocity at NFE ≤ 16 (Figure 1). A gap remains at low-temperature ($T = 0.1$) decoding, where MDLM and Duo reach 33–36% (Figure 3).

2 Background

Notation We denote by $\mathcal{V}$ the finite vocabulary of size $|\mathcal{V}|$. Boldface letters denote either sequences $\mathbf{x} \in \mathcal{V}^L$ of L tokens, with $\mathbf{x}^\ell$ the ℓ-th element, or vectors in $\mathbb{R}^d$, the meaning clear from context. We write $\mathbb{S}^{d-1} := \{\mathbf{x} \in \mathbb{R}^d : \|\mathbf{x}\| = 1\}$ for the unit hypersphere in $\mathbb{R}^d$, and $\mathcal{U}(\mathbb{S}^{d-1})$ for the uniform distribution on $\mathbb{S}^{d-1}$. Token embeddings are stored in a lookup table $\mathbf{E} \in \mathbb{R}^{|\mathcal{V}| \times d}$ and we write $\mathbf{e}_v \in \mathbb{R}^d$ for the row associated with $v \in \mathcal{V}$.

Language Modeling and Autoregressive Models Language models approximate the data distribution $p_{\text{data}} : \mathcal{V}^L \to [0, 1]$ over sequences with a density $p_\theta(\mathbf{x})$. AR models factorize $p_\theta(\mathbf{x}) = \prod_{\ell=1}^{L} p_\theta(\mathbf{x}^\ell \mid \mathbf{x}^{<\ell})$ using the chain rule of probability. This factorization enables exact likelihood training, but implies that inference is slow, as we generate tokens one by one, and that we cannot condition on future tokens.

2.1 Flow Generative Modeling

Continuous Normalizing Flows (CNFs) (Chen et al., 2018; Grathwohl et al., 2018) are generative models on $\mathbb{R}^d$. CNFs learn a continuous-time transport from a noise distribution $p_0 = p_{\text{noise}}$ to the data distribution $p_1 = p_{\text{data}}$. The time-dependent velocity field $u_t^\theta \colon \mathbb{R}^d \to \mathbb{R}^d$ induces the *flow* $\phi_t \colon \mathbb{R}^d \to \mathbb{R}^d$ by integration:

$$\frac{d}{dt}\phi_t(z_0) = u_t^\theta(\phi_t(z_0)), \quad \phi_0(z_0) = z_0, \tag{1}$$

The velocity field u_t^θ is parameterized by a neural network with continuously differentiable, bounded derivatives, so the ODE (1) has a unique solution (Coddington & Levinson, 1955). For $t \in [0, 1]$, the pushforward $p_t = [\phi_t]_\sharp\, p_0$ defines intermediate densities p_t, and the family $\{p_t\}_{t\in[0,1]}$ is called a *probability path* from p_0 to p_1. Integrating (1) up to t produces a sample $z_t = \phi_t(z_0) \sim p_t$.

Flow Matching Flow Matching (FM) (Lipman et al., 2023; Liu et al., 2022; Albergo & Vanden-Eijnden, 2023) is a method to learn the velocity field u_t^θ that transports p_0 to p_1 (Suppl. A). The *true* velocity u_t is typically expressed as an expectation:

$$u_t(z_t) = \int u_{t|1}(z_t \mid x)\, p_{1|t}(x \mid z_t)\, dx, \tag{2}$$

where $u_{t|1}$ is a *conditional* velocity, conditioned on $x \sim p_{\text{data}}$, and $p_{1|t}$ is the posterior given the noisy example z_t. Since $p_{1|t}$ is generally intractable, FM trains u_t^θ against $u_{t|1}$ instead. Let $\psi_{t|1}$ denote the *conditional* flow

associated with $u_{t|1}$. A common choice is the linear interpolation:

$$\psi_{t|1}(z_0 \mid x) = z_t = \alpha_t\, x + (1 - \alpha_t)\, z_0, \tag{3}$$

where $z_0 \sim p_0$ and $x \sim p_1$. $\alpha_t \colon [0,1] \to [0,1]$ is a monotonically increasing *noise schedule* with $\alpha_0 = 0$ and $\alpha_1 = 1$. The conditional velocity is given by the time derivative of $\psi_{t|1}$:

$$u_{t|1}(z_t \mid x) = \dot{\alpha}_t\, (x - z_0). \tag{4}$$

A key result in FM (Lipman et al., 2023) is that the minimizer of the *Conditional Flow Matching* (CFM) loss is the marginal velocity u_t (2):

$$\mathcal{L}_{\mathrm{CFM}}(\theta) = \mathbb{E}_{t\sim\mathcal{U}[0,1],\, z_0\sim p_0,\, x\sim p_1} \left\| u_t^\theta(z_t) - u_{t|1}(z_t \mid x) \right\|^2. \tag{5}$$

2.2 Geometry of the Hypersphere

We summarize the primitives we use on $\mathbb{S}^{d-1}$. For a thorough treatment of Riemannian geometry, see do Carmo (do Carmo, 1992). The *geodesic distance* between $\mathbf{p}, \mathbf{q} \in \mathbb{S}^{d-1}$ is the angle $d_{\mathbb{S}}(\mathbf{p}, \mathbf{q}) = \arccos(\mathbf{p}^\top \mathbf{q}) \in [0, \pi]$. The *tangent space* at $\mathbf{p}$ is $T_{\mathbf{p}}\mathbb{S}^{d-1} = \{\mathbf{v} \in \mathbb{R}^d : \mathbf{v}^\top \mathbf{p} = 0\}$. The *exponential map* $\exp_{\mathbf{p}} \colon T_{\mathbf{p}}\mathbb{S}^{d-1} \to \mathbb{S}^{d-1}$ moves $\mathbf{p}$ along the geodesic in direction $\mathbf{v}$ for arc length $\|\mathbf{v}\|$:

$$\exp_{\mathbf{p}}(\mathbf{v}) = \cos(\|\mathbf{v}\|)\, \mathbf{p} + \sin(\|\mathbf{v}\|)\, \frac{\mathbf{v}}{\|\mathbf{v}\|}. \tag{6}$$

The *logarithmic map* $\log_{\mathbf{p}} \colon \mathbb{S}^{d-1} \to T_{\mathbf{p}}\mathbb{S}^{d-1}$ inverts the exponential map and returns the tangent vector at $\mathbf{p}$ pointing toward $\mathbf{q}$, with magnitude $d_{\mathbb{S}}(\mathbf{p}, \mathbf{q})$[1]:

$$\log_{\mathbf{p}}(\mathbf{q}) = \frac{\omega}{\sin \omega}\, (\mathbf{q} - \cos(\omega)\, \mathbf{p}), \quad \omega = d_{\mathbb{S}}(\mathbf{p}, \mathbf{q}). \tag{7}$$

The *Spherical Linear Interpolation* (SLERP) follows the geodesic from $\mathbf{p}$ to $\mathbf{q}$ (Shoemake, 1985):

$$\mathrm{SLERP}(\mathbf{p}, \mathbf{q}, t) = \frac{\sin((1-t)\,\omega)}{\sin \omega}\, \mathbf{p} + \frac{\sin(t\,\omega)}{\sin \omega}\, \mathbf{q}, \quad \omega = d_{\mathbb{S}}(\mathbf{p}, \mathbf{q}), \tag{8}$$

or equivalently, $\mathrm{SLERP}(\mathbf{p}, \mathbf{q}, t) = \exp_{\mathbf{p}}\big(t\, \log_{\mathbf{p}}(\mathbf{q})\big)$. To sample uniformly on $\mathbb{S}^{d-1}$, draw $\boldsymbol{\epsilon} \sim \mathcal{N}(\mathbf{0}, \mathbf{I}_d)$ and normalize $\boldsymbol{\epsilon} \leftarrow \boldsymbol{\epsilon}/\|\boldsymbol{\epsilon}\|$ (Muller, 1959).

2.3 Flow Matching on the Hypersphere

Riemannian Flow Matching (RFM) (Chen & Lipman, 2024) extends FM to Riemannian manifolds, which include $\mathbb{S}^{d-1}$. As in the Euclidean case, the marginal velocity is the expectation of a conditional velocity:

$$u_t(\mathbf{z}_t) = \int u_{t|1}(\mathbf{z}_t \mid \mathbf{z}_1)\, p_{1|t}(\mathbf{z}_1 \mid \mathbf{z}_t)\, d\mathbf{z}_1, \tag{9}$$

where $u_{t|1}$ is the conditional velocity associated with the conditional flow $\psi_{t|1}$, and $p_{1|t}$ is the posterior given $\mathbf{z}_t$. We define $\psi_{t|1}$ with SLERP (8), where $\mathbf{z}_0 \sim p_0$ is drawn from a noise distribution on $\mathbb{S}^{d-1}$ and $\mathbf{z}_1 \sim p_1$ is a data sample:

$$\psi_{t|1}(\mathbf{z}_0 \mid \mathbf{z}_1) = \mathbf{z}_t = \mathrm{SLERP}(\mathbf{z}_0, \mathbf{z}_1, \alpha_t) = \exp_{\mathbf{z}_0}\big(\alpha_t\, \log_{\mathbf{z}_0}(\mathbf{z}_1)\big), \tag{10}$$

which satisfies $\psi_{0|1}(\mathbf{z}_0 \mid \mathbf{z}_1) = \mathbf{z}_0$ and $\psi_{1|1}(\mathbf{z}_0 \mid \mathbf{z}_1) = \mathbf{z}_1$. Differentiating $\psi_{t|1}$ gives the conditional velocity (Suppl. A.2):

$$u_{t|1}(\mathbf{z}_t \mid \mathbf{z}_1) = \frac{\dot{\alpha}_t}{1 - \alpha_t}\, \log_{\mathbf{z}_t}(\mathbf{z}_1). \tag{11}$$

As in the Euclidean case, the minimizer of the Riemannian Conditional Flow Matching (RCFM) loss is the marginal velocity u_t (9):

$$\mathcal{L}_{\mathrm{RCFM}}(\theta) = \mathbb{E}_{t\sim\mathcal{U}[0,1],\, \mathbf{z}_0\sim p_0,\, \mathbf{z}_1\sim p_1} \left\| u_t^\theta(\mathbf{z}_t) - u_{t|1}(\mathbf{z}_t \mid \mathbf{z}_1) \right\|^2. \tag{12}$$

[1] When $\mathbf{p} = -\mathbf{q}$ (antipodal points), $\log_{\mathbf{p}}(\mathbf{q})$ is undefined since infinitely many geodesics connect them.

3 Hyperspherical Flow Language Models

Figure 2 overviews the training and sampling. $\mathbb{S}$-FLM is a Riemannian CNF on $(\mathbb{S}^{d-1})^L$ that transports a sequence of random vectors on $\mathbb{S}^{d-1}$ towards the clean token representation. To bridge the continuous and discrete representations, we map tokens to the sphere via a normalized embedding lookup and decode via the arg max of $p^\theta_{1|t}$. The denoiser $p^\theta_{1|t}$, trained with cross-entropy, induces a closed-form marginal velocity field that we integrate at sampling time. Optionally, after each optimization step, we re-project the embeddings to $\mathbb{S}^{d-1}$ (Suppl. B.5).

Encoder and Decoder Let $\mathbf{x} = (x^1, \ldots, x^L) \in \mathcal{V}^L$ be an input sequence of L tokens. Each token $v \in \mathcal{V}$ is associated with a unit-norm embedding $\hat{\mathbf{e}}_v \in \mathbb{S}^{d-1}$, hence we represent $\mathbf{x}$ as a sequence in $(\mathbb{S}^{d-1})^L$. The decoder $g\colon (\mathbb{S}^{d-1})^L \times [0,1] \to \mathcal{V}^L$ is defined as the arg max of the learned posterior:

$$\mathbf{e}_v = \mathbf{E}[v], \qquad \hat{\mathbf{e}}_v = \frac{\mathbf{e}_v}{\|\mathbf{e}_v\|_2}, \qquad g^\ell(\mathbf{z}, t) = \arg\max_{v \in \mathcal{V}} p^\theta_{1|t}(\mathbf{x}^\ell = v \mid \mathbf{z}), \tag{13}$$

Training with Cross-Entropy Unlike standard flow matching on fixed data (e.g., pixels), we train the data representation via an embedding table $\mathbf{E}$ jointly with the flow by backpropagating through the SLERP. Regressing the velocity field against learnable embeddings admits a trivial minimum where all token representations collapse to a point. Instead, we approximate the posterior $p_{1|t}(\cdot \mid \mathbf{z}_t)$ with a denoiser $p^\theta_{1|t}(\cdot \mid \mathbf{z}_t)$, trained with cross-entropy (CE). The denoiser cannot recover the clean token if embeddings collapse, thus the CE pushes them apart, as noted in CDCD (Dieleman et al., 2022). At every position ℓ, we take $\mathbf{z}^\ell_1 = \hat{\mathbf{e}}_{\mathbf{x}^\ell}$ (13) as the clean endpoint, draw $\mathbf{z}^\ell_0 \sim \mathcal{U}(\mathbb{S}^{d-1})$ independently, and form the noisy latent $\mathbf{z}^\ell_t = \mathrm{SLERP}(\mathbf{z}^\ell_0, \mathbf{z}^\ell_1, \alpha_t)$ (10). We minimize the cross-entropy

$$\mathcal{L}_{\mathrm{CE}}(\theta) = \mathbb{E}_{\mathbf{x} \sim p_1,\, t \sim \mathcal{U}[0,1],\, \mathbf{z}_0 \sim p_0} \left[-\sum_{\ell=1}^{L} \log p^\theta_{1|t}(\mathbf{x}^\ell \mid \mathbf{z}_t) \right]. \tag{14}$$

3.1 Sampling

Exact velocity Because our data distribution is supported on $\{\hat{\mathbf{e}}_v : v \in \mathcal{V}\}^L \subset (\mathbb{S}^{d-1})^L$, the marginal velocity (9) reduces to a finite sum at each position:

$$u^\theta_t(\mathbf{z}^\ell_t) = \frac{\dot{\alpha}_t}{1 - \alpha_t} \sum_{v \in \mathcal{V}} p^\theta_{1|t}(\mathbf{x}^\ell = v \mid \mathbf{z}_t)\, \log_{\mathbf{z}^\ell_t}(\hat{\mathbf{e}}_v)\,. \tag{15}$$

We call this the *exact velocity*, in contrast to the stochastic and top-k approximations below.

Stochastic decoding We can replace the sum in (15) with a single Monte Carlo sample of the posterior. At each step, we draw $\hat{\mathbf{x}}^\ell \sim p^\theta_{1|t}(\cdot \mid \mathbf{z}_t)$ and use $\bar{\mathbf{v}}^\ell = \log_{\mathbf{z}^\ell_t}(\hat{\mathbf{e}}_{\hat{\mathbf{x}}^\ell})$ in place of (15). The deterministic and stochastic samplers differ only in how they construct the velocity from $p^\theta_{1|t}$. CANDI (Pynadath et al., 2025) uses an analogous one-sample Monte Carlo approximation. See Algo. 3 for the pseudocode.

Top-k velocity Alternatively, we can restrict the sum in (15) to the top-k entries of $p^\theta_{1|t}(\cdot \mid \mathbf{z}_t)$ at each sampling step. We take the top-k logits and apply log-softmax to renormalize over the truncated set. We call this *top-k velocity decoding*, with $k = 1$ giving *top*-1 decoding, the analogue of greedy decoding for autoregressive models.

Temperature scaling The three velocity variants depend on the posterior $p^\theta_{1|t}(\cdot \mid \mathbf{z}_t)$. To control sampling diversity, we apply a temperature $T > 0$ to the logits ℓ_v of $p^\theta_{1|t}$:

$$p^{\theta,T}_{1|t}(v \mid \mathbf{z}_t) \propto \exp(\ell_v / T). \tag{16}$$

When sampling with scaled temperature, we substitute $p^{\theta,T}_{1|t}$ for $p^\theta_{1|t}$ in the exact, stochastic, and top-k velocities.

3.2 Noise Schedule

Truncation After training with standard noise schedules (Table 5), we observe that $p^{\theta}_{1|t}$ becomes close to one-hot in few sampling steps. This is likely due to the *curse of dimensionality* (Bellman, 1961). In high dimension, $\mathbb{S}^{d-1}$ has enough room to spread $|\mathcal{V}|$ embeddings apart (Vershynin, 2018). Training with CE separates the embeddings because the denoiser cannot differentiate tokens whose embeddings coincide (Wang & Isola, 2020). When the embeddings are well separated, the true posterior $p_{1|t}$ at low noise levels (α_t large) is close to one-hot. Thus, during sampling, after $\mathbf{z}^{\ell}_t$ enters the Voronoi cell of a clean embedding $\hat{\mathbf{e}}_k$, the posterior collapses. To avoid training on noise levels where $p_{1|t}$ is close to one-hot, we truncate the noise schedule to $[0, a] \subseteq [0, 1]$, i.e. we train only at the higher noise levels. We propose a closed-form expression for the truncation bound a as a function of the vocabulary size $|\mathcal{V}|$ and embedding dimension d by analyzing a tractable approximation of the sampling dynamics on $\mathbb{S}^{d-1}$. Truncation is critical for strong performance, as seen in Sudoku (Table 1), and after a grid search on GSM8K, our bound achieves similar accuracy as the best truncation value (Suppl. C.6).

Tractable model of the sampling dynamics. Let $\{\hat{\mathbf{e}}_v\}_{v\in\mathcal{V}}$ be the normalized token representations, sampled i.i.d. uniformly on $\mathbb{S}^{d-1}$. Let $\mathbf{z}_0 \sim \mathcal{U}(\mathbb{S}^{d-1})$ be the initial noise sample. Fix a target token k and let $\mathbf{z}_\alpha = \mathrm{SLERP}(\mathbf{z}_0, \hat{\mathbf{e}}_k, \alpha)$ for $\alpha \in [0, 1]$. Define $\alpha^\star(\delta)$ as the smallest α at which $\hat{\mathbf{e}}_k$ is the nearest neighbor of $\mathbf{z}_\alpha$ with probability at least $1 - \delta$. Then, in high dimension,

$$\alpha^\star(\delta) \approx \frac{2}{\pi} \arcsin\left(\sqrt{\frac{2\log\big(2(|\mathcal{V}| - 1)/\delta\big)}{d}}\right). \tag{17}$$

Derivation sketch. Under our model, the similarity to non-target tokens $\langle \mathbf{z}_\alpha, \hat{\mathbf{e}}_v\rangle$ (with $v \neq k$) is sub-Gaussian, as the product of a fixed vector and a uniform random vector on $\mathbb{S}^{d-1}$ (Vershynin, 2018). With a simple union bound, we conclude that $\max_{v\neq k}\langle \mathbf{z}_\alpha, \hat{\mathbf{e}}_v\rangle \leq \sqrt{2\log(2(|\mathcal{V}| - 1)/\delta)/d}$ with probability at least $1 - \delta$. Along the sampling trajectory, $\langle \mathbf{z}_\alpha, \hat{\mathbf{e}}_k\rangle = \cos((1 - \alpha)\omega)$ with $\omega = d_{\mathbb{S}}(\mathbf{z}_0, \hat{\mathbf{e}}_k) \approx \pi/2$ in high dimension, thus $\langle \mathbf{z}_\alpha, \hat{\mathbf{e}}_k\rangle \approx \sin(\pi\alpha/2)$. We conclude by solving for the critical point such that $\mathbf{z}_\alpha$ is closest to $\hat{\mathbf{e}}_v$ with high probability. The complete argument is in Suppl. C.2, and the numerical values in Table 4. □

Adaptive noise schedule On top of truncating to $[0, a]$, we adapt the noise schedule during training to allocate more samples to noise levels where the loss $\mathcal{L}$ changes most, inspired by InfoNoise (Raya et al., 2026). Every 50 steps, we fit the loss profile $\hat{\mathcal{L}}(t)$ from recent pairs $(t, \mathcal{L})$ and define the noise schedule α_t using the inverse CDF of $|d\hat{\mathcal{L}}/dt|$ (Dieleman et al., 2022). We use $|d\hat{\mathcal{L}}/dt|$ as a proxy for the critical noise levels where the model learns most, thus sample these more often. We stabilize the updates with an *exponential moving average* (EMA) of the successive schedules. Find the pseudocode and comparison with InfoNoise in Suppl. B.2. In practice, the adaptive schedule does not slow training (Table 3).

3.3 Hyperspherical Architecture

The latents $\mathbf{z}^{\ell}_t$ live on $\mathbb{S}^{d-1}$, and the sampling step (15) rotates vectors. We propose a Transformer variant inspired by nGPT (Loshchilov et al., 2024) that keeps the intermediate activations on $\mathbb{S}^{d-1}$ and parameterizes the attention and MLP layers as rotations. Each block replaces the additive residual with a normalized interpolation $\mathbf{h}_{\text{out}} \leftarrow \mathrm{Norm}\big(\mathbf{h}_{\text{in}} + \boldsymbol{\gamma} \odot (\mathrm{Norm}(\mathbf{h}_{\text{layer}}) - \mathbf{h}_{\text{in}})\big)$, where $\mathbf{h}_{\text{in}}$ is the input, $\mathbf{h}_{\text{layer}}$ is the layer (MLP or attention) output, and $\mathbf{h}_{\text{out}}$ is the updated state. The normalized interpolation approximates SLERP for small $\boldsymbol{\gamma}$. The per-dimension gate $\boldsymbol{\gamma}$ is computed from the noise level, similar to adaptive layernorm (adaLN) in DiT (Peebles & Xie, 2023). We do not use adaLN, so our architecture ($\mathbb{S}$-*arch*) has slightly *fewer* parameters than the standard DiT used in discrete diffusion papers (Sahoo et al., 2024; 2025a; 2026). The $\mathbb{S}$-arch achieves better results over the standard DiT (Sec. 4).

Takeaway. We propose the $\mathbb{S}$-arch to implement the denoiser $p^{\theta}_{1|t}$ in place of the standard DiT. We train with cross-entropy (14) with a truncated, adaptive noise schedule. We marginalize the conditional velocities under $p^{\theta}_{1|t}$ to obtain u^{θ}_t (15) and integrate from $\mathbf{z}_0 \sim p_0$ to $\mathbf{z}_1$, and decode with $\arg\max$. The velocity admits exact, stochastic, and top-k variants. See Algo. 1, Algo. 2, and Algo. 3 for pseudocode.

4 Experiments

We apply $\mathbb{S}$-FLM to Sudoku solving (Sec. 4.1), math reasoning via code on TinyGSM (Liu et al., 2023) (Sec. 4.2), and unconditional language modeling on OWT (Gokaslan & Cohen, 2019) (Sec. 4.3). The most common measure of sample quality in recent work on diffusion language models is *Generative Perplexity* (Gen. PPL) and is computed using a large AR model. However, samples with good likelihood are not necessarily correct at the sequence level (Veličković et al., 2026; Feng et al., 2025), and repetitive text has low perplexity (Dieleman et al., 2022; Deschenaux & Gulcehre, 2024). Therefore, we primarily focus on datasets with ground-truth solutions (Sudoku, GSM8K).

4.1 Reasoning on Sudoku

Experimental Setup We compare $\mathbb{S}$-FLM with AR and recent diffusion models on Sudoku (Ben-Hamu et al., 2025; Kim et al., 2025). We use 48k training and 2k validation puzzles (no overlap), each with a unique solution (Alp, 2024). We define three difficulty levels, based on the number of visible digits (easy: 40/81, medium: 35/81, hard: 30/81). We use the modified *Diffusion Transformer* (DiT) (Peebles & Xie, 2023) architecture from SEDD (Lou et al., 2024) with 8 layers and embedding dimension 512. We compare against AR, MDLM (Sahoo et al., 2024), Duo (Sahoo et al., 2025a), CANDI (Pynadath et al., 2025), and FLM (Lee et al., 2026), using 180 sampling steps for the diffusion variants. We describe the input format and training hyperparameters in Suppl. C.3.

Table 1: Exact match accuracy (%) on Sudoku when sampling with 180 steps. The overall best is underlined. The best score with continuous diffusion is **bolded**. CANDI is a hybrid continuous-masked model, which can also be trained as a pure Gaussian diffusion model. $\mathbb{S}$-FLM is best, but similar to FLM.

Model	Easy	Med.	Hard
Autoregressive			
Sample	13.9	5.1	0.6
Greedy	14.6	5.1	1.0
Discrete Diffusion			
MDLM (Sahoo et al., 2024)	92.0	77.1	30.2
Duo (Sahoo et al., 2025a)	96.3	84.7	58.4
Continuous Diffusion			
CANDI (Pynadath et al., 2025)	79.3	45.9	16.7
CANDI pure Gaussian	63.9	41.9	12.5
FLM (Lee et al., 2026)	94.2	82.7	44.5
$\mathbb{S}$-FLM	81.5	50.6	14.0
$\mathbb{S}$-FLM+ $\alpha^\star(0.1)$	94.0	77.6	43.2
$\mathbb{S}$-FLM+ $\alpha^\star(0.1)$ + adaptive	**94.8**	**85.2**	**45.0**

Results Table 1 shows the results. The autoregressive model performs poorly on all difficulties, since the task requires global context. Duo (Sahoo et al., 2025a) obtains the highest accuracy. Among the continuous methods, FLM (Lee et al., 2026) and $\mathbb{S}$-FLM outperform AR and MDLM at every difficulty. $\mathbb{S}$-FLM with the simple linear schedule performs poorly on hard Sudokus, but with truncation and the adaptive schedule, $\mathbb{S}$-FLM performs similarly to the prior best continuous language models. See Suppl. C.4 for the ablation over schedules and embedding re-projection. We do not re-project embeddings to $\mathbb{S}^{d-1}$ after each optimizer step in Table 1.

4.2 Reasoning on GSM8K

Experimental Setup TinyGSM (Liu et al., 2023) is a dataset of $\sim$ 11.8M synthetic math word problems similar to GSM8K (Cobbe et al., 2021). Each solution is a GPT-3.5-generated Python program that produces the numerical answer. We compare our models in the GSM8K test, after executing one generated solution per problem. We plot error bars corresponding to bootstrapped confidence intervals in the percentile 95% on the test set (Suppl. C.5). We use the `SmolLM-135M` tokenizer (Allal et al., 2025) because it compresses the code better than the GPT-2 tokenizer (Radford et al., 2019) (Figure 5). We pad the input sequences to length 512 and compute the loss on padding tokens. As for Sudoku, we always keep the problem statement

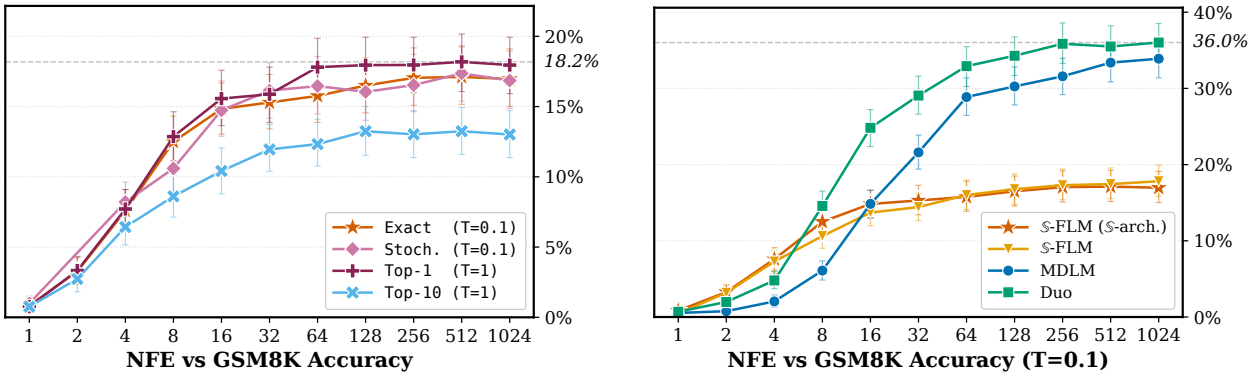

Figure 3: **Accuracy on GSM8K with $T = 0.1$. Left:** Decoding strategies for 𝕊-FLM (𝕊-arch). At low temperature, sampling with the exact or stochastic velocities approaches the accuracy with top-1 decoding. **Right:** At $T = 0.1$ the standard DiT and the 𝕊-arch perform similarly, and their accuracy is roughly half of that of Duo. At $T = 1$ the 𝕊-arch outperforms the standard DiT (Figure 6).

clean, so that we can sample conditionally. All backbones use hidden dimension 768, 12 layers, 12 attention heads, and dropout 0.1. For 𝕊-FLM, we train both the standard DiT and the 𝕊-arch (Sec. 3.3). We train for 250k steps with batch size 512, using Adam (lr $= 3 \times 10^{-4}$, $\beta_1 = 0.9$, $\beta_2 = 0.999$, no weight decay) and an EMA rate of 0.9999.

Table 2: Accuracy (%) on GSM8K after 250k training steps. Diffusion variants use 1024 steps, no temperature scaling, AR uses 512 (context length). The overall best is underlined, the best continuous diffusion result is **bolded**. 𝕊-FLM outperforms prior continuous diffusion language models, and **closes the gap to MDLM at $T = 1$ when the velocity (15) is computed with top-$k = 1$.** A gap remains at low-temperature ($T = 0.1$) decoding, where MDLM and Duo reach 33–36% (Figure 3).

Model	Acc. (%)
Autoregressive	
Sample	53.9
Greedy	63.3
Discrete Diffusion	
MDLM (Sahoo et al., 2024)	18.0
DUO (Sahoo et al., 2025a)	17.2
Continuous Diffusion	
CANDI (Pynadath et al., 2025)	0.2
FLM (Lee et al., 2026)	0.3
𝕊-FLM	1.2
+ $\alpha^\star(0.1)$	7.7
+ no renorm.	8.1
+ adaptive	11.1
+ 𝕊-arch. (Sec. 3.3)	12.4
+ top-$k = 1$	**18.0**

Results We report the accuracy at $T = 1$ with 1024 sampling steps for diffusion variants in Table 2. The accuracy of CANDI (Pynadath et al., 2025) and FLM (Lee et al., 2026) is below 1% despite using their respective optimized schedules. Temperature annealing did not improve the accuracy above 0.5%. In contrast, 𝕊-FLM solves 18% of problems with top-1 decoding. In Table 2, we ablate on the impact of each new element of 𝕊-FLM. With the vanilla linear schedule, 𝕊-FLM has an accuracy of 1.2%.

The truncation of the noise schedule according to (17) improves to 7.7%. *Not* re-normalizing the embeddings after each optimization step (Suppl. B.5) increases it to 8.1%. Note that the denoiser always processes unit-norm vectors in the forward pass, but the embedding table itself can either be re-projected to $\mathbb{S}^{d-1}$ after every optimization step or left unconstrained. Skipping the re-projection is equivalent to annealing learning rate for embedding vectors (Suppl. B.5), which might stabilize training since the velocity (15) is a function of the embeddings. The adaptive noise schedule improves the accuracy to 11.1% and 𝕊-arch to 12.4%. With top-$k = 1$ velocity decoding (15), 𝕊-FLM closes the gap to MDLM and Duo at $T = 1$. A gap remains at low-temperature ($T = 0.1$) decoding, where MDLM and Duo reach 33–36% (Figure 3).

Ablations Figure 1 shows that at $T = 1$, with NFE ≤ 16, 𝕊-FLM outperforms MDLM and Duo. All methods benefit from greedy decoding (Sec. 3.1); therefore, we compare 𝕊-FLM with MDLM, Duo at low temperature ($T = 0.1$). At $T = 0.1$, MDLM reaches 33% and Duo 36%, while 𝕊-FLM is around 18% (Figure 3). Thus, while 𝕊-FLM outperforms previous continuous approaches,

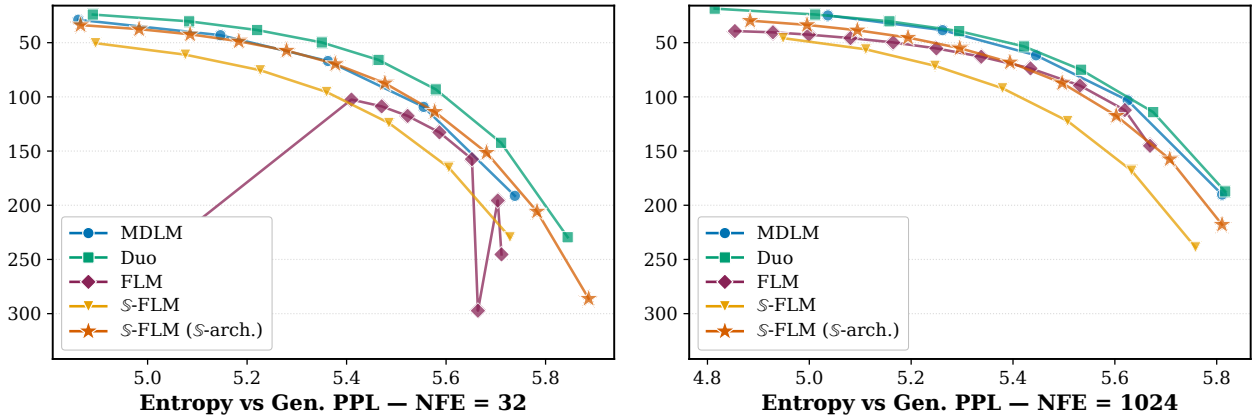

Figure 4: **Gen. PPL (↓) / Entropy (↑) Frontier on OpenWebText** at NFE = 32 (left) and NFE = 1024 (right). Each curve is obtained by sweeping over the temperature T. $\mathbb{S}$-FLM with the $\mathbb{S}$-arch performs similarly to prior FLMs. Duo is best overall. At NFE = 32, the frontier of FLM is highly unstable.

there is a large performance gap at low temperature compared to discrete diffusion and AR. Figure 8 shows that at $T = 1$, the only k such that top-k decoding significantly improves the accuracy is $k = 1$. In addition, the top-1 decoding beats the low-temperature and the stochastic sampler (Figure 9). See Suppl. C.7 for more details.

4.3 Language Modeling on OpenWebText

Experimental Setup Following MDLM (Sahoo et al., 2024), we train $\mathbb{S}$-FLM on OpenWebText using the GPT-2 tokenizer and a context length of 1024. The model is a 12-layer standard DiT backbone with hidden dimension 768 and 12 attention heads. We train for 1M steps with the same optimizer configuration as in TinyGSM (Sec. 4.2). For FLM (Lee et al., 2026), we use the original checkpoint released by the authors.

Gen. PPL / Entropy Frontier Repetitive generations can improve the Gen. PPL without improving sample quality (Veličković et al., 2026), and different models might have different optimal sampling temperatures. We therefore evaluate the Gen. PPL and the average unigram entropy across $T \in \{0.70, 0.75, \ldots, 1.20\}$ and plot the frontier for each model and NFE (details in Suppl. C.8) (Pynadath et al., 2025). In NFE = 1024 (right), $\mathbb{S}$-FLM with the $\mathbb{S}$-arch matches prior FLMs in Gen. PPL, while the standard DiT is slightly weaker. At low NFE, the frontier becomes unstable for prior FLMs, but remains stable for $\mathbb{S}$-FLM, which has a similar Gen. PPL to MDLM. Duo generally achieves the best Gen. PPL / Entropy trade-off. See Suppl. C.9 for the complete sweep of NFEs.

5 Related Work

$\mathbb{S}$-FLM differs from prior work in three ways: it operates in continuous rather than discrete space, defines its flow on the hypersphere $\mathbb{S}^{d-1}$, and learns token embeddings end-to-end.

Continuous diffusion for language modeling Prior work applies Gaussian diffusion to embeddings and trains end-to-end with cross-entropy (Li et al., 2022; Gulrajani & Hashimoto, 2023), or regresses onto pre-trained embeddings (Strudel et al., 2022; Lovelace et al., 2022; Shen et al., 2026), which caps sample quality at the pre-trained embeddings and requires two training stages. Riemannian flow models extend score-based generative modeling to manifolds (Mathieu & Nickel, 2020; Bortoli et al., 2022; Lou et al., 2023), but generally assume data already lie on the manifold. $\mathbb{S}$-FLM instead learns the embeddings and the velocity on $\mathbb{S}^{d-1}$ jointly and injects noise via rotations.

Flow language models (FLMs) A recent line of work treats language modeling as flow matching on continuous representations. Several recent works (Sahoo et al., 2025a; Lee et al., 2026; Roos et al., 2026; Potaptchik et al., 2026) add Gaussian noise to one-hot or simplex representations and decode via arg max. These approaches materialize dense $L \times |\mathcal{V}|$ arrays at training and sampling time. Fisher-Flow (Davis et al., 2024) maps one-hot vectors to the positive orthant of $\mathbb{S}^{d-1}$ via the Fisher–Rao metric, but such approach does not scale well to language modeling with large vocabularies (Jo & Hwang, 2025). $\mathbb{S}$-FLM operates on d-dimensional token embeddings on $\mathbb{S}^{d-1}$, learned end-to-end, which avoids the $|\mathcal{V}|$-dimensional bottleneck and trains faster (Table 3).

Representation learning on the hypersphere Hyperspherical representations are common in contrastive learning, where uniform spread on $\mathbb{S}^{d-1}$ correlates with strong downstream performance (Wang & Isola, 2020), and the cosine distance outperform Euclidean one for comparing word embeddings (Mikolov et al., 2013; Pennington et al., 2014) and for retrieval (Reimers & Gurevych, 2019; Karpukhin et al., 2020). A latent prior on $\mathbb{S}^{d-1}$ also stabilizes Variational Autoencoders (Davidson et al., 2018; Xu & Durrett, 2018), and normalizing activations and weights to $\mathbb{S}^{d-1}$ improves the stability of AR models (Loshchilov et al., 2024). Suppl. D gives a fuller discussion.

6 Conclusion

We introduced $\mathbb{S}$-FLM, a Riemannian flow on $\mathbb{S}^{d-1}$ that is competitive at language modeling with large vocabularies and learns the velocity and embeddings jointly. Beyond the formalism, our key contributions include the $\mathbb{S}$-arch backbone with normalized activations and the truncated and adaptive noise-schedule analysis. On Sudoku, $\mathbb{S}$-FLM performs similarly to prior FLMs. On GSM8K, where other FLMs fail, $\mathbb{S}$-FLM with top-1 decoding closes the gap to MDLM and Duo at $T = 1$, though a gap remains at low-temperature ($T = 0.1$) sampling. On OpenWebText, $\mathbb{S}$-FLM follows the Gen. PPL / Entropy frontier of prior FLMs at high NFE and beats them at low NFE where prior continuous models have an unstable frontier. $\mathbb{S}$-FLM avoids materializing $|\mathcal{V}|$-dimensional one-hot vectors, so it trains faster than prior FLMs and may be easier to scale (though this is speculation and left for future work). Our analysis of the sampling-dynamics provides a principled heuristic for truncating the noise schedule that works well in practice. At the same time, there remains a clear gap between diffusion models and AR models in GSM8K.

7 Limitations

Continuous diffusion language models, including $\mathbb{S}$-FLM, underperform their discrete counterparts. In TinyGSM, $\mathbb{S}$-FLM reduces the gap compared to prior FLMs but does not eliminate it, and a substantial gap to autoregressive decoding remains (Sec. 4.2). The truncation threshold $\alpha^\star(\delta)$ is derived a simplified model (Suppl. C.2) which assumes that the embeddings are randomly distributed on the sphere. The learned embeddings are likely more structured. Therefore, $\alpha^\star(\delta)$ should only be treated as a principled heuristic for the truncation hyperparameter. A more sophisticated model of the sampling dynamics might improve the bound. The $\mathbb{S}$-arch follows the design of nGPT for simplicity and trains slower than the standard DiT. Improving its throughput is an important future direction. The training dynamics of $\mathbb{S}$-FLM should also be studied further, and the results of contrastive representation learning may be relevant. We train a single model per configuration. Training once on TinyGSM costs more than $300, thus we could not afford to train several copies with the same hyperparameters.

8 Impact Statement

This work advances research on continuous diffusion language models. Like any language modeling research, it carries the standard risks of misuse for misinformation or harmful content. Our models are trained at small scale on Sudoku, TinyGSM (synthetc math word problems), and OpenWebText, and remain far below the capabilities of state-of-the-art autoregressive language models. Anyone seeking to cause harm has stronger publicly available models at their disposal. The contribution is methodological.

References

Michael S. Albergo and Eric Vanden-Eijnden. Building normalizing flows with stochastic interpolants, 2023. URL https://arxiv.org/abs/2209.15571.

Loubna Ben Allal, Anton Lozhkov, Elie Bakouch, Gabriel Martín Blázquez, Guilherme Penedo, Lewis Tunstall, Andrés Marafioti, Hynek Kydlíček, Agustín Piqueres Lajarín, Vaibhav Srivastav, Joshua Lochner, Caleb Fahlgren, Xuan-Son Nguyen, Clémentine Fourrier, Ben Burtenshaw, Hugo Larcher, Haojun Zhao, Cyril Zakka, Mathieu Morlon, Colin Raffel, Leandro von Werra, and Thomas Wolf. Smollm2: When smol goes big – data-centric training of a small language model, 2025. URL https://arxiv.org/abs/2502.02737.

Ali Alp. Sudoku puzzle generator. https://github.com/alicommit-malp/sudoku, 2024.

Marianne Arriola, Aaron Gokaslan, Justin T. Chiu, Zhihan Yang, Zhixuan Qi, Jiaqi Han, Subham Sekhar Sahoo, and Volodymyr Kuleshov. Block diffusion: Interpolating between autoregressive and diffusion language models, 2025. URL https://arxiv.org/abs/2503.09573.

Jacob Austin, Daniel D. Johnson, Jonathan Ho, Daniel Tarlow, and Rianne van den Berg. Structured denoising diffusion models in discrete state-spaces, 2023. URL https://arxiv.org/abs/2107.03006.

Richard Bellman. *Adaptive Control Processes: A Guided Tour*. Princeton University Press, Princeton, NJ, 1961.

Heli Ben-Hamu, Itai Gat, Daniel Severo, Niklas Nolte, and Brian Karrer. Accelerated sampling from masked diffusion models via entropy bounded unmasking, 2025. URL https://arxiv.org/abs/2505.24857.

Valentin De Bortoli, Emile Mathieu, Michael Hutchinson, James Thornton, Yee Whye Teh, and Arnaud Doucet. Riemannian score-based generative modelling, 2022. URL https://arxiv.org/abs/2202.02763.

Andrew Campbell, Joe Benton, Valentin De Bortoli, Tom Rainforth, George Deligiannidis, and Arnaud Doucet. A continuous time framework for discrete denoising models, 2022. URL https://arxiv.org/abs/2205.14987.

Andrew Campbell, Jason Yim, Regina Barzilay, Tom Rainforth, and Tommi Jaakkola. Generative flows on discrete state-spaces: Enabling multimodal flows with applications to protein co-design, 2024. URL https://arxiv.org/abs/2402.04997.

Ricky T. Q. Chen and Yaron Lipman. Flow matching on general geometries, 2024. URL https://arxiv.org/abs/2302.03660.

Tian Qi Chen, Yulia Rubanova, Jesse Bettencourt, and David Kristjanson Duvenaud. Neural ordinary differential equations. *NeurIPS 2018*, abs/1806.07366, 2018.

Ting Chen, Ruixiang Zhang, and Geoffrey Hinton. Analog bits: Generating discrete data using diffusion models with self-conditioning, 2022. URL https://arxiv.org/abs/2208.04202.

Karl Cobbe, Vineet Kosaraju, Mohammad Bavarian, Mark Chen, Heewoo Jun, Lukasz Kaiser, Matthias Plappert, Jerry Tworek, Jacob Hilton, Reiichiro Nakano, Christopher Hesse, and John Schulman. Training verifiers to solve math word problems, 2021. URL https://arxiv.org/abs/2110.14168.

Earl A. Coddington and Norman Levinson. *Theory of Ordinary Differential Equations*. McGraw-Hill, New York, 1955.

Tim R. Davidson, Luca Falorsi, Nicola De Cao, Thomas Kipf, and Jakub M. Tomczak. Hyperspherical variational auto-encoders, 2018. URL https://arxiv.org/abs/1804.00891.

Oscar Davis, Samuel Kessler, Mircea Petrache, İsmail İlkan Ceylan, Michael Bronstein, and Avishek Joey Bose. Fisher flow matching for generative modeling over discrete data, 2024. URL https://arxiv.org/abs/2405.14664.

Justin Deschenaux and Caglar Gulcehre. Promises, outlooks and challenges of diffusion language modeling, 2024. URL https://arxiv.org/abs/2406.11473.

Justin Deschenaux, Lan Tran, and Caglar Gulcehre. Partition generative modeling: Masked modeling without masks, 2025. URL https://arxiv.org/abs/2505.18883.

Justin Deschenaux, Caglar Gulcehre, and Subham Sekhar Sahoo. The diffusion duality, chapter ii: ψ-samplers and efficient curriculum, 2026. URL https://arxiv.org/abs/2602.21185.

Prafulla Dhariwal and Alexander Nichol. Diffusion models beat gans on image synthesis. *Advances in neural information processing systems*, 34:8780–8794, 2021.

Sander Dieleman, Laurent Sartran, Arman Roshannai, Nikolay Savinov, Yaroslav Ganin, Pierre H. Richemond, Arnaud Doucet, Robin Strudel, Chris Dyer, Conor Durkan, Curtis Hawthorne, Rémi Leblond, Will Grathwohl, and Jonas Adler. Continuous diffusion for categorical data, 2022. URL https://arxiv.org/abs/2211.15089.

Manfredo Perdigão do Carmo. *Riemannian Geometry*. Mathematics: Theory & Applications. Birkhäuser Boston, 1992.

Bradley Efron. Bootstrap methods: Another look at the jackknife. *The Annals of Statistics*, 7(1):1–26, 1979.

Floor Eijkelboom, Grigory Bartosh, Christian Andersson Naesseth, Max Welling, and Jan-Willem van de Meent. Variational flow matching for graph generation, 2025. URL https://arxiv.org/abs/2406.04843.

Guhao Feng, Yihan Geng, Jian Guan, Wei Wu, Liwei Wang, and Di He. Theoretical benefit and limitation of diffusion language model, 2025. URL https://arxiv.org/abs/2502.09622.

F. N. Fritsch and J. Butland. A method for constructing local monotone piecewise cubic interpolants. *SIAM Journal on Scientific and Statistical Computing*, 5(2):300–304, 1984. doi: 10.1137/0905021.

Itai Gat, Tal Remez, Neta Shaul, Felix Kreuk, Ricky T. Q. Chen, Gabriel Synnaeve, Yossi Adi, and Yaron Lipman. Discrete flow matching, 2024. URL https://arxiv.org/abs/2407.15595.

Gemini Team, Rohan Anil, Sebastian Borgeaud, et al. Gemini: A family of highly capable multimodal models, 2025. URL https://arxiv.org/abs/2312.11805.

Aaron Gokaslan and Vanya Cohen. Openwebtext corpus. http://Skylion007.github.io/OpenWebTextCorpus, 2019.

Google. Gemma 3 technical report, 2025. URL https://arxiv.org/abs/2503.19786.

Will Grathwohl, Ricky T. Q. Chen, Jesse Bettencourt, Ilya Sutskever, and David Duvenaud. Ffjord: Free-form continuous dynamics for scalable reversible generative models, 2018. URL https://arxiv.org/abs/1810.01367.

Ishaan Gulrajani and Tatsunori B. Hashimoto. Likelihood-based diffusion language models, 2023. URL https://arxiv.org/abs/2305.18619.

Xiaochuang Han, Sachin Kumar, and Yulia Tsvetkov. Ssd-lm: Semi-autoregressive simplex-based diffusion language model for text generation and modular control, 2023. URL https://arxiv.org/abs/2210.17432.

Jonathan Ho and Tim Salimans. Classifier-free diffusion guidance, 2022. URL https://arxiv.org/abs/2207.12598.

Jonathan Ho, Ajay Jain, and Pieter Abbeel. Denoising diffusion probabilistic models, 2020. URL https://arxiv.org/abs/2006.11239.

Jaehyeong Jo and Sung Ju Hwang. Continuous diffusion model for language modeling, 2025. URL https://arxiv.org/abs/2502.11564.

Mingyu Jo, Jaesik Yoon, Justin Deschenaux, Caglar Gulcehre, and Sungjin Ahn. Loopholing discrete diffusion: Deterministic bypass of the sampling wall, 2025. URL https://arxiv.org/abs/2510.19304.

Jared Kaplan, Sam McCandlish, Tom Henighan, Tom B. Brown, Benjamin Chess, Rewon Child, Scott Gray, Alec Radford, Jeffrey Wu, and Dario Amodei. Scaling laws for neural language models, 2020. URL https://arxiv.org/abs/2001.08361.

Vladimir Karpukhin, Barlas Oğuz, Sewon Min, Patrick Lewis, Ledell Wu, Sergey Edunov, Danqi Chen, and Wen tau Yih. Dense passage retrieval for open-domain question answering, 2020. URL https://arxiv.org/abs/2004.04906.

Tero Karras, Miika Aittala, Jaakko Lehtinen, Janne Hellsten, Timo Aila, and Samuli Laine. Analyzing and improving the training dynamics of diffusion models, 2024. URL https://arxiv.org/abs/2312.02696.

Jaeyeon Kim, Seunggeun Kim, Taekyun Lee, David Z. Pan, Hyeji Kim, Sham Kakade, and Sitan Chen. Fine-tuning masked diffusion for provable self-correction, 2025. URL https://arxiv.org/abs/2510.01384.

Diederik P. Kingma and Jimmy Ba. Adam: A method for stochastic optimization, 2017. URL https://arxiv.org/abs/1412.6980.

Ouail Kitouni, Niklas Nolte, Diane Bouchacourt, Adina Williams, Mike Rabbat, and Mark Ibrahim. The factorization curse: Which tokens you predict underlie the reversal curse and more, 2024. URL https://arxiv.org/abs/2406.05183.

Chanhyuk Lee, Jaehoon Yoo, Manan Agarwal, Sheel Shah, Jerry Huang, Aditi Raghunathan, Seunghoon Hong, Nicholas M. Boffi, and Jinwoo Kim. One-step language modeling via continuous denoising, 2026. URL https://arxiv.org/abs/2602.16813.

Xiang Lisa Li, John Thickstun, Ishaan Gulrajani, Percy Liang, and Tatsunori B. Hashimoto. Diffusion-lm improves controllable text generation, 2022. URL https://arxiv.org/abs/2205.14217.

Yaron Lipman, Ricky T. Q. Chen, Heli Ben-Hamu, Maximilian Nickel, and Matt Le. Flow matching for generative modeling, 2023. URL https://arxiv.org/abs/2210.02747.

Bingbin Liu, Sebastien Bubeck, Ronen Eldan, Janardhan Kulkarni, Yuanzhi Li, Anh Nguyen, Rachel Ward, and Yi Zhang. TinyGSM: Achieving >80% on GSM8k with small language models, 2023. URL https://arxiv.org/abs/2312.09241.

Xingchao Liu, Chengyue Gong, and Qiang Liu. Flow straight and fast: Learning to generate and transfer data with rectified flow, 2022. URL https://arxiv.org/abs/2209.03003.

Ilya Loshchilov, Cheng-Ping Hsieh, Simeng Sun, and Boris Ginsburg. ngpt: Normalized transformer with representation learning on the hypersphere, 2024. URL https://arxiv.org/abs/2410.01131.

Aaron Lou, Derek Lim, Isay Katsman, Leo Huang, Qingxuan Jiang, Ser-Nam Lim, and Christopher De Sa. Neural manifold ordinary differential equations, 2020. URL https://arxiv.org/abs/2006.10254.

Aaron Lou, Minkai Xu, and Stefano Ermon. Scaling riemannian diffusion models, 2023. URL https://arxiv.org/abs/2310.20030.

Aaron Lou, Chenlin Meng, and Stefano Ermon. Discrete diffusion modeling by estimating the ratios of the data distribution, 2024. URL https://arxiv.org/abs/2310.16834.

Justin Lovelace, Varsha Kishore, Chao Wan, Eliot Shekhtman, and Kilian Q. Weinberger. Latent diffusion for language generation, 2022. URL https://arxiv.org/abs/2212.09462.

Rabeeh Karimi Mahabadi, Hamish Ivison, Jaesung Tae, James Henderson, Iz Beltagy, Matthew E. Peters, and Arman Cohan. TESS: Text-to-text self-conditioned simplex diffusion, 2023. URL https://arxiv.org/abs/2305.08379.

Emile Mathieu and Maximilian Nickel. Riemannian continuous normalizing flows, 2020. URL https://arxiv.org/abs/2006.10605.

Meta. The llama 3 herd of models, 2024. URL https://arxiv.org/abs/2407.21783.

Tomas Mikolov, Kai Chen, Greg Corrado, and Jeffrey Dean. Efficient estimation of word representations in vector space, 2013. URL https://arxiv.org/abs/1301.3781.

Mervin E. Muller. A note on a method for generating points uniformly on n-dimensional spheres. *Communications of the ACM*, 2(4):19–20, 1959.

Vaishnavh Nagarajan, Chen Henry Wu, Charles Ding, and Aditi Raghunathan. Roll the dice & look before you leap: Going beyond the creative limits of next-token prediction. *arXiv preprint arXiv:2504.15266*, 2025.

Shen Nie, Fengqi Zhu, Chao Du, Tianyu Pang, Qian Liu, Guangtao Zeng, Min Lin, and Chongxuan Li. Scaling up masked diffusion models on text, 2025. URL https://arxiv.org/abs/2410.18514.

Hunter Nisonoff, Junhao Xiong, Stephan Allenspach, and Jennifer Listgarten. Unlocking guidance for discrete state-space diffusion and flow models. *arXiv preprint arXiv:2406.01572*, 2024.

OpenAI. Gpt-4 technical report, 2024a. URL https://arxiv.org/abs/2303.08774.

OpenAI. Gpt-oss: open-weight language models by openai. https://github.com/openai/gpt-oss, 2024b. GitHub repository.

Vassilis Papadopoulos, Jérémie Wenger, and Clément Hongler. Arrows of time for large language models, 2024. URL https://arxiv.org/abs/2401.17505.

William Peebles and Saining Xie. Scalable diffusion models with transformers, 2023. URL https://arxiv.org/abs/2212.09748.

Jeffrey Pennington, Richard Socher, and Christopher Manning. GloVe: Global vectors for word representation. In *Proceedings of the 2014 Conference on Empirical Methods in Natural Language Processing (EMNLP)*, pp. 1532–1543. Association for Computational Linguistics, 2014. URL https://aclanthology.org/D14-1162/.

Peter Potaptchik, Jason Yim, Adhi Saravanan, Peter Holderrieth, Eric Vanden-Eijnden, and Michael S. Albergo. Discrete flow maps, 2026. URL https://arxiv.org/abs/2604.09784.

Patrick Pynadath, Jiaxin Shi, and Ruqi Zhang. Candi: Hybrid discrete-continuous diffusion models, 2025. URL https://arxiv.org/abs/2510.22510.

Qwen Team. Qwen2.5 technical report, 2025. URL https://arxiv.org/abs/2412.15115.

Alec Radford, Jeff Wu, Rewon Child, David Luan, Dario Amodei, and Ilya Sutskever. Language models are unsupervised multitask learners, 2019.

Sebastian Raschka. Creating confidence intervals for machine learning classifiers. https://sebastianraschka.com/blog/2022/confidence-intervals-for-ml.html, 2022. Accessed 2026-05-05.

Gabriel Raya, Bac Nguyen, Georgios Batzolis, Yuhta Takida, Dejan Stancevic, Naoki Murata, Chieh-Hsin Lai, Yuki Mitsufuji, and Luca Ambrogioni. Information-guided noise allocation for efficient diffusion training, 2026. URL https://arxiv.org/abs/2602.18647.

Nils Reimers and Iryna Gurevych. Sentence-bert: Sentence embeddings using siamese bert-networks, 2019. URL https://arxiv.org/abs/1908.10084.

Daan Roos, Oscar Davis, Floor Eijkelboom, Michael Bronstein, Max Welling, İsmail İlkan Ceylan, Luca Ambrogioni, and Jan-Willem van de Meent. Categorical flow maps, 2026. URL https://arxiv.org/abs/2602.12233.

Subham Sekhar Sahoo, Marianne Arriola, Yair Schiff, Aaron Gokaslan, Edgar Marroquin, Justin T Chiu, Alexander Rush, and Volodymyr Kuleshov. Simple and effective masked diffusion language models, 2024. URL https://arxiv.org/abs/2406.07524.

Subham Sekhar Sahoo, Justin Deschenaux, Aaron Gokaslan, Guanghan Wang, Justin Chiu, and Volodymyr Kuleshov. The diffusion duality, 2025a. URL https://arxiv.org/abs/2506.10892.

Subham Sekhar Sahoo, Zhihan Yang, Yash Akhauri, Johnna Liu, Deepansha Singh, Zhoujun Cheng, Zhengzhong Liu, Eric Xing, John Thickstun, and Arash Vahdat. Esoteric language models, 2025b. URL https://arxiv.org/abs/2506.01928.

Subham Sekhar Sahoo, Jean-Marie Lemercier, Zhihan Yang, Justin Deschenaux, Jingyu Liu, John Thickstun, and Ante Jukic. Scaling beyond masked diffusion language models, 2026. URL https://arxiv.org/abs/2602.15014.

Yair Schiff, Subham Sekhar Sahoo, Hao Phung, Guanghan Wang, Sam Boshar, Hugo Dalla-torre, Bernardo P. de Almeida, Alexander Rush, Thomas Pierrot, and Volodymyr Kuleshov. Simple guidance mechanisms for discrete diffusion models, 2025. URL https://arxiv.org/abs/2412.10193.

Junzhe Shen, Jieru Zhao, Ziwei He, and Zhouhan Lin. Codar: Continuous diffusion language models are more powerful than you think, 2026. URL https://arxiv.org/abs/2603.02547.

Jiaxin Shi, Kehang Han, Zhe Wang, Arnaud Doucet, and Michalis K. Titsias. Simplified and generalized masked diffusion for discrete data, 2025. URL https://arxiv.org/abs/2406.04329.

Ken Shoemake. Animating rotation with quaternion curves. In *Proceedings of the 12th Annual Conference on Computer Graphics and Interactive Techniques*, SIGGRAPH '85, New York, NY, USA, 1985. Association for Computing Machinery. ISBN 0897911660. doi: 10.1145/325334.325242. URL https://doi.org/10.1145/325334.325242.

Jascha Sohl-Dickstein, Eric A. Weiss, Niru Maheswaranathan, and Surya Ganguli. Deep unsupervised learning using nonequilibrium thermodynamics, 2015. URL https://arxiv.org/abs/1503.03585.

Hannes Stark, Bowen Jing, Chenyu Wang, Gabriele Corso, Bonnie Berger, Regina Barzilay, and Tommi Jaakkola. Dirichlet flow matching with applications to dna sequence design, 2024. URL https://arxiv.org/abs/2402.05841.

Robin Strudel, Corentin Tallec, Florent Altché, Yilun Du, Yaroslav Ganin, Arthur Mensch, Will Grathwohl, Nikolay Savinov, Sander Dieleman, Laurent Sifre, and Rémi Leblond. Self-conditioned embedding diffusion for text generation, 2022. URL https://arxiv.org/abs/2211.04236.

Jianlin Su, Yu Lu, Shengfeng Pan, Ahmed Murtadha, Bo Wen, and Yunfeng Liu. Roformer: Enhanced transformer with rotary position embedding, 2023. URL https://arxiv.org/abs/2104.09864.

Alexander Tong, Kilian Fatras, Nikolay Malkin, Guillaume Huguet, Yanlei Zhang, Jarrid Rector-Brooks, Guy Wolf, and Yoshua Bengio. Improving and generalizing flow-based generative models with minibatch optimal transport, 2024. URL https://arxiv.org/abs/2302.00482.

Ashish Vaswani, Noam Shazeer, Niki Parmar, Jakob Uszkoreit, Llion Jones, Aidan N. Gomez, Lukasz Kaiser, and Illia Polosukhin. Attention is all you need, 2023. URL https://arxiv.org/abs/1706.03762.

Petar Veličković, Federico Barbero, Christos Perivolaropoulos, Simon Osindero, and Razvan Pascanu. Perplexity cannot always tell right from wrong, 2026. URL https://arxiv.org/abs/2601.22950.

Roman Vershynin. *High-Dimensional Probability: An Introduction with Applications in Data Science*. Number 47 in Cambridge Series in Statistical and Probabilistic Mathematics. Cambridge University Press, 2018.

Dimitri von Rütte, Janis Fluri, Yuhui Ding, Antonio Orvieto, Bernhard Schölkopf, and Thomas Hofmann. Generalized interpolating discrete diffusion, 2025. URL https://arxiv.org/abs/2503.04482.

Dimitri von Rütte, Janis Fluri, Omead Pooladzandi, Bernhard Schölkopf, Thomas Hofmann, and Antonio Orvieto. Scaling behavior of discrete diffusion language models, 2026. URL https://arxiv.org/abs/2512.10858.

Tongzhou Wang and Phillip Isola. Understanding contrastive representation learning through alignment and uniformity on the hypersphere, 2020. URL https://arxiv.org/abs/2005.10242.

Chengyue Wu, Hao Zhang, Shuchen Xue, Zhijian Liu, Shizhe Diao, Ligeng Zhu, Ping Luo, Song Han, and Enze Xie. Fast-dllm: Training-free acceleration of diffusion llm by enabling kv cache and parallel decoding, 2025. URL https://arxiv.org/abs/2505.22618.

Jiacheng Xu and Greg Durrett. Spherical latent spaces for stable variational autoencoders, 2018. URL https://arxiv.org/abs/1808.10805.

Olga Zaghen, Floor Eijkelboom, Alison Pouplin, Cong Liu, Max Welling, Jan-Willem van de Meent, and Erik J. Bekkers. Riemannian variational flow matching for material and protein design, 2026. URL https://arxiv.org/abs/2502.12981.

Daniel Zhang-Li, Nianyi Lin, Jifan Yu, Zheyuan Zhang, Zijun Yao, Xiaokang Zhang, Lei Hou, Jing Zhang, and Juanzi Li. Reverse that number! decoding order matters in arithmetic learning, 2024. URL https://arxiv.org/abs/2403.05845.

Contents

1 Introduction **1**

2 Background **3**

2.1 Flow Generative Modeling . . . 3

2.2 Geometry of the Hypersphere . . . 4

2.3 Flow Matching on the Hypersphere . . . 4

3 Hyperspherical Flow Language Models **5**

3.1 Sampling . . . 5

3.2 Noise Schedule . . . 6

3.3 Hyperspherical Architecture . . . 6

4 Experiments **7**

4.1 Reasoning on Sudoku . . . 7

4.2 Reasoning on GSM8K . . . 7

4.3 Language Modeling on OpenWebText . . . 9

5 Related Work **9**

6 Conclusion **10**

7 Limitations **11**

8 Impact Statement **11**

A Background on Flow Matching **19**

A.1 The Continuity Equation . . . 19

A.2 Deriving the Conditional Velocity Fields . . . 19

B Additional Details **20**

B.1 Training and Sampling Pseudocode . . . 20

B.2 Adaptive Noise Schedule . . . 20

B.3 Hyperspherical Backbone Architecture . . . 22

B.4 Step Size with the Euler Sampler . . . 23

B.5 Re-Normalizing Embeddings . . . 23

B.6 Training Cost . . . 24

C Additional Results **24**

C.1 Sequence Length Using Different Tokenizers . . . 24

C.2 Analysis under the Random Codebook Model 25
C.3 Sudoku Setup 27
C.4 Additional Ablations on Sudoku 27
C.5 Bootstrap Confidence Intervals on TinyGSM 28
C.6 Additional Ablations on TinyGSM 28
C.7 Additional Sampling Results on TinyGSM 29
C.8 Gen. PPL / Entropy Frontier Protocol 31
C.9 Additional Results on OpenWebText 32

D Extended Related Work **33**

A Background on Flow Matching

A.1 The Continuity Equation

The velocity field u_t and the density p_t are related locally through the *continuity equation*:

$$\partial_t p_t + \nabla \cdot (p_t\, u_t) = 0. \tag{18}$$

This guarantees that matching u_t suffices to match p_t, without computing ϕ_t or its Jacobian. The Flow Matching (FM) objective regresses u_t^θ against a target velocity field:

$$\mathcal{L}_{\mathrm{FM}}(\theta) = \mathbb{E}_{t\sim\mathcal{U}[0,1],\, x\sim p_t} \left\| u_t^\theta(x) - u_t(x) \right\|^2. \tag{19}$$

In general, u_t and p_t are intractable. CFM replaces them with tractable conditional quantities. Differentiating the conditional flow $x_t = \alpha_t x_1 + (1-\alpha_t)x_0$ yields the conditional velocity field $u_{t|1}(x_t \mid x_1) = \dot{\alpha}_t(x_1 - x_0)$. The marginal velocity field is recovered by averaging under the posterior:

$$u_t(x) = \int u_{t|1}(x \mid x_1)\, \frac{p_{t|1}(x \mid x_1)\, q(x_1)}{p_t(x)}\, dx_1 = \int u_{t|1}(x \mid x_1)\, p_{1|t}(x_1 \mid x)\, dx_1. \tag{20}$$

The CFM objective has the same gradients and minimizer as $\mathcal{L}_{\mathrm{FM}}$ but is tractable (Lipman et al., 2023; Tong et al., 2024).

A.2 Deriving the Conditional Velocity Fields

Training both Euclidean and Riemannian flow models requires computing the conditional velocity field $u_{t|1}(\mathbf{z}_t \mid \mathbf{z}_1)$ that serves as the regression target in the CFM loss. In both cases, the derivation follows the same recipe: (1) define a conditional flow $\psi_{t|1}$, (2) differentiate with respect to t to obtain $\frac{d\mathbf{z}_t}{dt}$, and (3) eliminate $\mathbf{z}_0$ so that the velocity field is expressed as a function of the current position $\mathbf{z}_t$. During training, any equivalent form of the velocity field can be used as the regression target.

Euclidean Case We define the conditional flow (3) as the linear interpolation $x_t = \alpha_t\, x_1 + (1-\alpha_t)\, x_0$. Differentiating with respect to t:

$$\frac{dx_t}{dt} = \dot{\alpha}_t\, (x_1 - x_0). \tag{21}$$

By simple algebra, we find $x_0 = (x_t - \alpha_t\, x_1)/(1-\alpha_t)$. Substituting:

$$\begin{aligned} u_{t|1}(x_t \mid x_1) &= \dot{\alpha}_t \left(x_1 - \frac{x_t - \alpha_t\, x_1}{1-\alpha_t} \right) = \frac{\dot{\alpha}_t}{1-\alpha_t}(x_1(1-\alpha_t) - x_t + \alpha_t\, x_1) \\ &= \boxed{\frac{\dot{\alpha}_t}{1-\alpha_t}\,(x_1 - x_t).} \end{aligned} \tag{22}$$

For the common choice $\alpha_t = t$, this simplifies to $u_{t|1}(x_t \mid x_1) = (x_1 - x_t)/(1-t)$. During training, the equivalent form $u_{t|1}(x_t \mid x_1) = \dot{\alpha}_t\, (x_1 - x_0)$ can also be used.

Spherical Case Let $\omega = d_{\mathbb{S}}(\mathbf{z}_0, \mathbf{z}_1) \in (0, \pi)$ be the geodesic distance between the endpoints. The conditional flow (10), written using the SLERP formula (8), is

$$\mathbf{z}_t = \frac{\sin((1-\alpha_t)\,\omega)}{\sin\omega}\, \mathbf{z}_0 + \frac{\sin(\alpha_t\,\omega)}{\sin\omega}\, \mathbf{z}_1. \tag{23}$$

Differentiating with respect to t:

$$\frac{d\mathbf{z}_t}{dt} = \frac{\dot{\alpha}_t\,\omega}{\sin\omega}\left[-\cos((1-\alpha_t)\,\omega)\, \mathbf{z}_0 + \cos(\alpha_t\,\omega)\, \mathbf{z}_1\right]. \tag{24}$$

Algorithm 1 Training

Require: Dataset of token sequences, embedding table $\mathbf{E}$, scheduling function α_t

repeat
  Sample sequence $\mathbf{x} \sim p_1$, time $t \sim \mathcal{U}[0,1]$
  for $\ell = 1$ **to** L **do**
    $\mathbf{z}_1^\ell \leftarrow \mathbf{E}[\mathbf{x}^\ell]/\|\mathbf{E}[\mathbf{x}^\ell]\|$ ▷ Embed and normalize
    $\boldsymbol{\epsilon}^\ell \sim \mathcal{N}(\mathbf{0}, \mathbf{I}_d)$; $\mathbf{z}_0^\ell \leftarrow \boldsymbol{\epsilon}^\ell/\|\boldsymbol{\epsilon}^\ell\|$ ▷ Sample noise on $\mathbb{S}^{d-1}$
    $\mathbf{z}_t^\ell \leftarrow \mathrm{SLERP}(\mathbf{z}_0^\ell, \mathbf{z}_1^\ell, \alpha_t)$ ▷ Construct noisy latent
  end for
  Compute $\mathcal{L}_{\mathrm{CE}} = -\sum_\ell \log p^\theta_{1|t}(\mathbf{x}^\ell \mid \mathbf{z}_t)$ ▷ Cross-entropy loss
  Update θ and $\mathbf{E}$ by gradient descent on $\mathcal{L}_{\mathrm{CE}}$
until converged

Rewriting (23) gives $\mathbf{z}_0 = \frac{\sin\omega}{\sin((1-\alpha_t)\,\omega)}\,\mathbf{z}_t - \frac{\sin(\alpha_t\,\omega)}{\sin((1-\alpha_t)\,\omega)}\,\mathbf{z}_1$. Substituting into (24):

$$\frac{d\mathbf{z}_t}{dt} = \frac{\dot\alpha_t\,\omega}{\sin\omega}\left[-\frac{\cos((1-\alpha_t)\omega)\,\sin\omega}{\sin((1-\alpha_t)\omega)}\,\mathbf{z}_t + \frac{\cos((1-\alpha_t)\omega)\,\sin(\alpha_t\omega) + \cos(\alpha_t\omega)\,\sin((1-\alpha_t)\omega)}{\sin((1-\alpha_t)\omega)}\,\mathbf{z}_1\right]. \tag{25}$$

The numerator of the $\mathbf{z}_1$ coefficient simplifies by the following identity: $\cos((1-\alpha_t)\omega)\sin(\alpha_t\omega) + \cos(\alpha_t\omega)\sin((1-\alpha_t)\omega) = \sin\omega$. Therefore:

$$\frac{d\mathbf{z}_t}{dt} = \frac{\dot\alpha_t\,\omega}{\sin((1-\alpha_t)\,\omega)}\left(\mathbf{z}_1 - \cos((1-\alpha_t)\,\omega)\,\mathbf{z}_t\right). \tag{26}$$

Recalling the definition of the logarithmic map (7) with $d_{\mathbb{S}}(\mathbf{z}_t, \mathbf{z}_1) = (1-\alpha_t)\,\omega$, we recognize that (26) is proportional to $\log_{\mathbf{z}_t}(\mathbf{z}_1) = \frac{(1-\alpha_t)\,\omega}{\sin((1-\alpha_t)\,\omega)}(\mathbf{z}_1 - \cos((1-\alpha_t)\,\omega)\,\mathbf{z}_t)$. Their ratio is $\dot\alpha_t\omega/((1-\alpha_t)\omega) = \dot\alpha_t/(1-\alpha_t)$, giving

$$\boxed{u_{t|1}(\mathbf{z}_t \mid \mathbf{z}_1) = \frac{\dot\alpha_t}{1-\alpha_t}\,\log_{\mathbf{z}_t}(\mathbf{z}_1).} \tag{27}$$

During training, the equivalent form from (24) can also be used.

B Additional Details

B.1 Training and Sampling Pseudocode

Algo. 1 shows the training pseudocode for $\mathbb{S}$-FLM, Algo. 2 the deterministic sampler, and Algo. 3 the stochastic sampler that replaces the posterior-weighted velocity by the log map toward a single token sampled from $p^\theta_{1|t}$.

B.2 Adaptive Noise Schedule

Motivation The denoising task is not as meaningful at every noise level. At low noise levels, the task is trivial since the noisy embeddings are very close to the clean embeddings (17). At high noise levels, the latent $\mathbf{z}_t^\ell$ is close to pure noise hence carries little signal about the clean token. In both cases the denoiser $p^\theta_{1|t}$ has little to learn. The informative region lies in between, where the model can extract signal from noise and the loss drops fastest as a function of t. Inspired by InfoNoise (Raya et al., 2026), we focus training on regions where the loss derivative $|d\mathcal{L}/dt|$ is largest.

Algorithm 2 Sampling

Require: Denoiser $p^{\theta}_{1|t}$, embedding table $\mathbf{E}$ with rows $\mathbf{e}_v$ and unit-norm versions $\hat{\mathbf{e}}_v = \mathbf{e}_v/\|\mathbf{e}_v\|$, number of steps N, decoder p_{dec}

for $\ell = 1$ **to** L **do**
  $\boldsymbol{\epsilon}^{\ell} \sim \mathcal{N}(\mathbf{0}, \mathbf{I}_d)$; $\mathbf{z}^{\ell}_0 \leftarrow \boldsymbol{\epsilon}^{\ell}/\|\boldsymbol{\epsilon}^{\ell}\|$ ▷ Sample noise on $\mathbb{S}^{d-1}$
end for
for $n = 0$ **to** $N-1$ **do**
  $s_n \leftarrow (\alpha_{t_{n+1}} - \alpha_{t_n}) \,/\, (1 - \alpha_{t_n})$ ▷ Step size
  Compute $p^{\theta}_{1|t_n}(\cdot \mid \mathbf{z}_{t_n})$ ▷ One forward pass
  for $\ell = 1$ **to** L **do**
    $\bar{\mathbf{v}}^{\ell} \leftarrow \sum_{v \in \mathcal{V}} p^{\theta}_{1|t_n}(v \mid \mathbf{z}_{t_n}) \, \log_{\mathbf{z}^{\ell}_{t_n}}(\hat{\mathbf{e}}_v)$ ▷ Posterior-weighted velocity
    $\mathbf{z}^{\ell}_{t_{n+1}} \leftarrow \exp_{\mathbf{z}^{\ell}_{t_n}}\big(s_n \cdot \bar{\mathbf{v}}^{\ell}\big)$ ▷ Geodesic Euler step
  end for
end for
$\mathbf{x} \sim p_{\text{dec}}(\cdot \mid \mathbf{z}_1)$ ▷ Decode (argmax or AR)
return $\mathbf{x}$

Algorithm 3 Stochastic sampling

Require: Denoiser $p^{\theta}_{1|t}$, embedding table $\mathbf{E}$ with rows $\mathbf{e}_v$ and unit-norm versions $\hat{\mathbf{e}}_v = \mathbf{e}_v/\|\mathbf{e}_v\|$, number of steps N, decoder p_{dec}

for $\ell = 1$ **to** L **do**
  $\boldsymbol{\epsilon}^{\ell} \sim \mathcal{N}(\mathbf{0}, \mathbf{I}_d)$; $\mathbf{z}^{\ell}_0 \leftarrow \boldsymbol{\epsilon}^{\ell}/\|\boldsymbol{\epsilon}^{\ell}\|$ ▷ Sample noise on $\mathbb{S}^{d-1}$
end for
for $n = 0$ **to** $N-1$ **do**
  $s_n \leftarrow (\alpha_{t_{n+1}} - \alpha_{t_n}) \,/\, (1 - \alpha_{t_n})$ ▷ Step size
  Compute $p^{\theta}_{1|t_n}(\cdot \mid \mathbf{z}_{t_n})$ ▷ One forward pass
  for $\ell = 1$ **to** L **do**
    Sample $\hat{\mathbf{x}}^{\ell} \sim p^{\theta}_{1|t_n}(\cdot \mid \mathbf{z}_{t_n})$ ▷ Posterior sample
    $\bar{\mathbf{v}}^{\ell} \leftarrow \log_{\mathbf{z}^{\ell}_{t_n}}(\hat{\mathbf{e}}_{\hat{\mathbf{x}}^{\ell}})$ ▷ Velocity toward sampled token
    $\mathbf{z}^{\ell}_{t_{n+1}} \leftarrow \exp_{\mathbf{z}^{\ell}_{t_n}}\big(s_n \cdot \bar{\mathbf{v}}^{\ell}\big)$ ▷ Geodesic Euler step
  end for
end for
$\mathbf{x} \sim p_{\text{dec}}(\cdot \mid \mathbf{z}_1)$ ▷ Decode (argmax or AR)
return $\mathbf{x}$

Algorithm 4 Adaptive noise schedule refit

Require: buffer $\{(t_i, \mathcal{L}_i)\}$, base schedule α^{base}, grid $\{t_j\}_{j=1}^{N} \subset [0,1]$, EMA rate β, uniform mix μ, ridge λ, refit count n

Fit a spline $\hat{\mathcal{L}}(t)$ to $(t_i, \mathcal{L}_i)$ via ridge regression (λ)
$g(t_j) \leftarrow \max\{d\hat{\mathcal{L}}/dt\,(t_j),\, 0\}$ ▷ Clamp: loss should grow with noise
$w(t_j) \leftarrow (1-\mu)\, g(t_j) + \mu$ ▷ Ensure the CDF is invertible
$F(t_j) \leftarrow \sum_{j' \le j} w(t_{j'}) \big/ \sum_{j'} w(t_{j'})$ ▷ Empirical CDF (discrete points)
$\tilde{t}_j \leftarrow F^{-1}(t_j)$ via PCHIP interpolation ▷ Invert CDF
$\bar{\alpha}_j \leftarrow \beta\, \bar{\alpha}_j + (1-\beta)\, \alpha^{\text{base}}(\tilde{t}_j)$ ▷ EMA update
$\alpha^{\text{final}}_j \leftarrow \bar{\alpha}_j/(1-\beta^n)$ ▷ Bias correction
Store α^{adapt}_t as a PCHIP spline through $\{(t_j, \alpha^{\text{final}}_j)\}$

During training we append $(t, \mathcal{L})$ pairs to the buffer at every step and invoke Algo. 4 every R steps after a warmup of $W = 1000$ steps. The EMA is essential to reduce oscillations in the schedule, and the Adam-style

bias correction $1/(1-\beta^n)$ (Kingma & Ba, 2017) prevents the early-training estimate from being biased toward zero. By default we use $R = 50$, buffer size $R \cdot$ batch size, $\beta = 0.9$, and $\mu = 10^{-3}$. All operations run on CPU in `numpy`, so the impact on training throughput is minimal. Empirically, the noise schedule stabilizes quickly.

Implementation We fit the loss profile using a spline (`sklearn.preprocessing.SplineTransformer`) with ridge regression (`sklearn.linear_model.Ridge`). For interpolating the inverse CDF F^{-1} and the final noise schedule α_t^{adapt}, we use `scipy.interpolate.PchipInterpolator`, which builds a *Piecewise Cubic Hermite Interpolating Polynomial* (Fritsch & Butland, 1984) that preserves the monotonicity of the data.

Relation to InfoNoise Our adaptive schedule is inspired by InfoNoise (Raya et al., 2026), which also adapts the noise schedule online from the value of the loss. We differ in several ways.

- **Importance signal.** InfoNoise estimates the conditional entropy rate $\dot{H}[\mathbf{x}_0 \mid \mathbf{x}_\sigma] \propto \text{mmse}(\sigma)/\sigma^3$ via the I–MMSE identity. We use $|d\hat{\mathcal{L}}/dt|$ directly on the cross-entropy profile.
- **Estimator.** InfoNoise splits the σ-range into bins, each with a FIFO buffer for recent losses and an EMA on the MSE estimate. We fit a spline to $(t, \mathcal{L})$ pairs via ridge regression. This removes the need to choose a number of bins.
- **Stabilization.** InfoNoise uses pivot calibration and gating to suppress boundary artifacts. We enforce a minimum CDF increment μ to keep the CDF invertible and stabilize the schedule with an EMA, in addition to truncating the noise schedule range (17).
- **Loss weight.** InfoNoise separates sampling density $\pi(\sigma)$ from loss weight $w(\sigma)$ via the effective weight $\phi = \pi \cdot w$. We use unweighted cross-entropy ($w \equiv 1$), so the sampling density matches effective weight directly.

B.3 Hyperspherical Backbone Architecture

In this section, we present the hyperspherical denoising backbone in more details. The architecture is adapted from nGPT (Loshchilov et al., 2024) for $\mathbb{S}$-FLM. The main differences are that (1) we use bidirectional attention, (2) we use GELU activations in the MLP, since the other AR / diffusion denoisers also use GELU, (3) we make the residual gates time-conditional. As in nGPT, every weight matrix has unit-norm vectors along the embedding-dimension axis. We enforce this at initialization and optionally re-apply the projection after every optimizer step.

Notation Let $\text{Norm}(\mathbf{u}) = \mathbf{u}/\max(\|\mathbf{u}\|_2, \varepsilon)$ with $\varepsilon = 10^{-6}$ project a vector onto the unit sphere along its last axis. We write d for the embedding dimension, H for the number of attention heads, $d_k = d/H$, and N for the number of transformer blocks. The base scale $b = 1/\sqrt{d}$ appears in several rescaling parameters. All per-dimension scales $(\mathbf{s}_{qk}, \mathbf{s}_{fc}, \mathbf{s}_z)$ and residual gates $(\boldsymbol{\gamma}_A, \boldsymbol{\gamma}_M)$ introduced below are learnable.

Normalized attention The multi-head attention uses bias-free linear layers: $\mathbf{Q} = \mathbf{h}\mathbf{W}_Q$, $\mathbf{K} = \mathbf{h}\mathbf{W}_K$, $\mathbf{V} = \mathbf{h}\mathbf{W}_V$, split into H heads. RoPE (Su et al., 2023) is applied to $\mathbf{Q}, \mathbf{K}$. We then apply the normalization and rescaling:

$$\tilde{\mathbf{s}}_{qk} = \mathbf{s}_{qk} \cdot s_{qk}^{\text{init}}/s_{qk}^{\text{scale}}, \qquad \mathbf{Q}' = \tilde{\mathbf{s}}_{qk} \odot \text{Norm}(\mathbf{Q}), \quad \mathbf{K}' = \tilde{\mathbf{s}}_{qk} \odot \text{Norm}(\mathbf{K}),$$

with $s_{qk}^{\text{init}} = 1$ and $s_{qk}^{\text{scale}} = b$. The softmax scaling follows from the variance of the inner product $\langle \hat{\mathbf{q}}, \hat{\mathbf{k}} \rangle$ between two unit-norm vectors $\hat{\mathbf{q}} = \text{Norm}(\mathbf{Q})$ and $\hat{\mathbf{k}} = \text{Norm}(\mathbf{K})$. Assume the components of $\mathbf{Q}, \mathbf{K}$ are i.i.d. zero-mean Gaussian. After projection by Norm, $\hat{\mathbf{q}}$ and $\hat{\mathbf{k}}$ are independent samples from $\text{Unif}(\mathbb{S}^{d_k-1})$. By rotational symmetry and $\|\mathbf{u}\|^2 = 1$, any $\mathbf{u} \sim \text{Unif}(\mathbb{S}^{d_k-1})$ satisfies $\mathbb{E}[u_i] = 0$ and $\mathbb{E}[u_i u_j] = \delta_{ij}/d_k$, hence $\mathbb{E}[\langle \hat{\mathbf{q}}, \hat{\mathbf{k}} \rangle] = 0$ and $\text{Var}[\langle \hat{\mathbf{q}}, \hat{\mathbf{k}} \rangle] = 1/d_k$. Following nGPT, we therefore set the softmax scale to $\sqrt{d_k}$:

$$\mathbf{O} = \text{softmax}\big(\sqrt{d_k}\, \mathbf{Q}'\mathbf{K}'^\top\big)\mathbf{V}, \qquad \mathbf{h}_A = \mathbf{O}\,\mathbf{W}_O.$$

Normalized MLP The MLP is similar to the MLP in discrete-diffusion DiTs (Peebles & Xie, 2023; Lou et al., 2024), with the addition of a per-dimension scale $\mathbf{s}_{fc}$ on the hidden activations:

$$\mathbf{h}_M = \mathrm{GELU}\big(\sqrt{d}\,\mathbf{s}_{fc} \odot (\mathbf{h}\,\mathbf{W}_{fc})\big)\,\mathbf{W}_O^M.$$

As in the previous section, the $\sqrt{d}$ factor restores unit variance to the inputs of GELU.

Timestep injection Let $\boldsymbol{\tau}(t) = \mathrm{SiLU}(\mathrm{TimestepEmbedder}(\sigma(t))) \in \mathbb{R}^{d_{\mathrm{cond}}}$ be the timestep embedding (sinusoidal embedding followed by a two-layer MLP). Each transformer block has its own zero-initialized linear map $\mathbf{W}_{\boldsymbol{\delta}} \in \mathbb{R}^{2d \times d_{\mathrm{cond}}}$ that computes per-dimension biases $(\boldsymbol{\delta}_A(t), \boldsymbol{\delta}_M(t)) = \mathbf{W}_{\boldsymbol{\delta}}\boldsymbol{\tau}(t)$, for the residual update (next paragraph).

Residual update The block updates the hidden state by interpolating with the (normalized) attention output, and then with the (normalized) MLP output. Each interpolation is gated by learnable per-dimension parameters $\boldsymbol{\gamma}_A, \boldsymbol{\gamma}_M \in \mathbb{R}^d$, and renormalized:

$$\mathbf{h} \leftarrow \mathrm{Norm}\Big(\mathrm{Norm}(\mathbf{h}) + \tilde{\boldsymbol{\gamma}}_A \odot \big(\mathrm{Norm}(\mathbf{h}_A) - \mathrm{Norm}(\mathbf{h})\big)\Big),$$
$$\mathbf{h} \leftarrow \mathrm{Norm}\Big(\mathrm{Norm}(\mathbf{h}) + \tilde{\boldsymbol{\gamma}}_M \odot \big(\mathrm{Norm}(\mathbf{h}_M) - \mathrm{Norm}(\mathbf{h})\big)\Big).$$

The effective gate is $\tilde{\boldsymbol{\gamma}}_X = |\boldsymbol{\gamma}_X \cdot (\gamma^{\mathrm{init}}/\gamma^{\mathrm{scale}}) + \boldsymbol{\delta}_X(t)|$ with $\gamma^{\mathrm{init}} = 0.05$ and $\gamma^{\mathrm{scale}} = b$, for $X \in \{A, M\}$, where $\boldsymbol{\delta}_X(t)$ is the time modulation defined above. Except for the time modulation $\boldsymbol{\delta}_X(t)$, the design and hyperparameters, are carried from nGPT. The absolute value ensures the gate is non-negative, so the update always pulls $\mathbf{h}$ toward the block output.

Output head We project the output of the last block through a row-normalized linear map $\mathbf{W}_{\mathrm{lm}} \in \mathbb{R}^{|\mathcal{V}| \times d}$ and rescale by a learnable scale $\mathbf{s}_z \in \mathbb{R}^{|\mathcal{V}|}$:

$$\tilde{\mathbf{s}}_z = \mathbf{s}_z \cdot s_z^{\mathrm{init}}/s_z^{\mathrm{scale}}, \qquad \boldsymbol{\ell} = \tilde{\mathbf{s}}_z \odot (\mathbf{h}\,\mathbf{W}_{\mathrm{lm}}^\top),$$

with $s_z^{\mathrm{init}} = 1$ and $s_z^{\mathrm{scale}} = b$. The rescaling is necessary because $\mathbf{h}\mathbf{W}_{\mathrm{lm}}^\top$ contains inner products of unit vectors and is therefore bounded in $[-1, 1]^{|\mathcal{V}|}$. Without $\mathbf{s}_z$ the cross-entropy would saturate near a uniform distribution.

B.4 Step Size with the Euler Sampler

The marginal velocity from (15) is $u_t^\ell = \frac{\dot{\alpha}_t}{1-\alpha_t}\,\bar{u}_t^\ell$, where $\bar{u}_t^\ell = \sum_v p_{1|t}(\mathbf{x}^\ell = v \mid \mathbf{z}_t)\,\log_{\mathbf{z}_t^\ell}(\hat{\mathbf{e}}_v)$. During sampling, to take an Euler step of size Δt from time time t_n to t_{n+1}, we compute

$$\mathbf{z}_{t_{n+1}}^\ell = \exp_{\mathbf{z}_{t_n}^\ell}\big(\Delta t \cdot u_{t_n}^\ell\big) = \exp_{\mathbf{z}_{t_n}^\ell}\left(\frac{\dot{\alpha}_{t_n}\,\Delta t}{1-\alpha_{t_n}} \cdot \bar{u}_{t_n}^\ell\right). \tag{28}$$

Using the first-order approximation $\dot{\alpha}_{t_n}\,\Delta t \approx \alpha_{t_{n+1}} - \alpha_{t_n}$, the step size applied to $\bar{u}_t^\ell$ is

$$s_n = \frac{\alpha_{t_{n+1}} - \alpha_{t_n}}{1-\alpha_{t_n}}, \tag{29}$$

so that $\mathbf{z}_{t_{n+1}}^\ell = \exp_{\mathbf{z}_{t_n}^\ell}(s_n \cdot \bar{u}_{t_n}^\ell)$. For the linear schedule $\alpha_t = t$ with uniform time steps $t_n = n/N$, this gives $s_n = 1/(N-n)$.

B.5 Re-Normalizing Embeddings

We show that when embeddings are normalized during the forward pass, the norm of the embeddings grow at every optimization step, and thus we obtain a decay of the effective learning rate (since the angular updates become smaller). Our argument is similar to prior work (Karras et al., 2024).

Setup Let $\mathbf{e} \in \mathbb{R}^d$ be an *unconstrained* embedding vector, and let $\hat{\mathbf{e}} = \mathbf{e}/\|\mathbf{e}\|$ be the normalized version used in the forward pass. The loss $\mathcal{L}$ depends on $\mathbf{e}$ only through $\hat{\mathbf{e}}$.

Jacobian of the normalization The Jacobian of $\hat{\mathbf{e}}$ with respect to $\mathbf{e}$ is

$$\frac{\partial \hat{\mathbf{e}}}{\partial \mathbf{e}} = \frac{1}{\|\mathbf{e}\|} \left(\mathbf{I} - \hat{\mathbf{e}}\,\hat{\mathbf{e}}^\top\right). \tag{30}$$

By the chain rule, the gradient of $\mathcal{L}$ with respect to the unnormalized embedding is

$$\nabla_{\mathbf{e}}\mathcal{L} = \left(\frac{\partial \hat{\mathbf{e}}}{\partial \mathbf{e}}\right)^\top \nabla_{\hat{\mathbf{e}}}\mathcal{L} = \frac{1}{\|\mathbf{e}\|} \left(\mathbf{I} - \hat{\mathbf{e}}\,\hat{\mathbf{e}}^\top\right) \nabla_{\hat{\mathbf{e}}}\mathcal{L}, \tag{31}$$

where we used the fact that $\mathbf{I} - \hat{\mathbf{e}}\,\hat{\mathbf{e}}^\top$ is symmetric.

The gradient is orthogonal to e The matrix $\mathbf{P} = \mathbf{I} - \hat{\mathbf{e}}\,\hat{\mathbf{e}}^\top$ projects onto the subspace orthogonal to $\hat{\mathbf{e}}$. Since $\mathbf{e} = \|\mathbf{e}\|\,\hat{\mathbf{e}}$:

$$\begin{aligned}
\mathbf{e}^\top \nabla_{\mathbf{e}}\mathcal{L} &= \frac{1}{\|\mathbf{e}\|}\, \mathbf{e}^\top \left(\mathbf{I} - \hat{\mathbf{e}}\,\hat{\mathbf{e}}^\top\right) \nabla_{\hat{\mathbf{e}}}\mathcal{L} \\
&= \frac{1}{\|\mathbf{e}\|} \left(\mathbf{e}^\top - \underbrace{\mathbf{e}^\top \hat{\mathbf{e}}}_{=\|\mathbf{e}\|}\, \hat{\mathbf{e}}^\top\right) \nabla_{\hat{\mathbf{e}}}\mathcal{L} \\
&= \frac{1}{\|\mathbf{e}\|} \left(\mathbf{e}^\top - \|\mathbf{e}\|\,\hat{\mathbf{e}}^\top\right) \nabla_{\hat{\mathbf{e}}}\mathcal{L} \\
&= \frac{1}{\|\mathbf{e}\|} \left(\mathbf{e}^\top - \mathbf{e}^\top\right) \nabla_{\hat{\mathbf{e}}}\mathcal{L} = 0,
\end{aligned} \tag{32}$$

where we used $\|\mathbf{e}\|\,\hat{\mathbf{e}} = \mathbf{e}$.

Norm growth Since $\nabla_{\mathbf{e}}\mathcal{L} \perp \mathbf{e}$, a gradient step $\mathbf{e}' = \mathbf{e} - \eta\,\nabla_{\mathbf{e}}\mathcal{L}$ gives, by the Pythagorean theorem:

$$\|\mathbf{e}'\|^2 = \|\mathbf{e}\|^2 + \eta^2\,\|\nabla_{\mathbf{e}}\mathcal{L}\|^2 > \|\mathbf{e}\|^2. \tag{33}$$

The norm grows at every step, which induces an effective learning rate decay on the embedding table.

Fix After each optimization step, we can re-project $\mathbf{e} \leftarrow \mathbf{e}/\|\mathbf{e}\|$ (not through the computational graph, but by directly modifying the parameters). This ensures that $\|\mathbf{e}\| = 1$ and that there is no implicit learning rate annealing(Karras et al., 2024). Empirically, we find that the learning rate annealing on the embedding table is beneficial.

B.6 Training Cost

Training on Sudokus is fast and cheap. We use a single L40S GPU and train for less than 2 hours. Using the on-demand price on RunPod (`https://www.runpod.io`), training costs less than $2.

Table 3 shows the step per second and total cost on TinyGSM and OpenWebText. We train on H100 GPUs with bfloat16 mixed precision. We use 8 H100s for TinyGSM, and 16 H100s on OpenWebtext. We train for 250k steps on TinyGSM (Sec. 4.2) and 1M on OpenWebText (Sec. 4.3).

C Additional Results

C.1 Sequence Length Using Different Tokenizers

In Figure 5, we plot the histogram of length of the tokenized examples in TinyGSM (Liu et al., 2023), when tokenized with the GPT-2 tokenizer (Radford et al., 2019) or the SmolLM tokenizer (Allal et al., 2025). Since the SmolLM tokenizer was trained on code, unlike GPT-2, we see that it offers better compression. Therefore, for the experiments on TinyGSM, we use the SmolLM tokenizer.

Table 3: **Training cost** on TinyGSM and OpenWebText. The total duration and GPU-hours are derived from the step/sec. We did not investigate deeply why $\mathbb{S}$-FLM trains faster than MDLM. We did not try to hyper-optimize our implementations. For MDLM, CANDI and $\mathbb{S}$-FLM, we import their original implementation, based on the Duo codebase (https://github.com/s-sahoo/duo), since we also use it. It is plausible that MDLM / Duo can be made to train as fast as $\mathbb{S}$-FLM. Observe that FLM is slower than $\mathbb{S}$-FLM. This is expected since FLM materializes dense one-hot-diffused arrays, and multiplies them with the embedding table, which is costly.

	Steps/sec		Duration (h)		GPU-hours	
Model	TinyGSM	OWT	TinyGSM	OWT	TinyGSM	OWT
AR	5.4	6.0	12.8	46.6	102.1	745.7
MDLM	3.0	3.5	22.8	80.3	182.7	1284.5
Duo	3.0	3.5	22.8	80.3	182.7	1284.5
CANDI	3.0	2.5	23.5	108.9	188.3	1742.9
FLM	3.2	3.3	21.7	84.2	173.6	1346.8
$\mathbb{S}$-FLM	4.2	4.5	16.5	61.7	132.3	987.7
$\mathbb{S}$-FLM + adapt.	4.2	4.5	16.5	61.7	132.3	987.7
$\mathbb{S}$-FLM + adapt. + $\mathbb{S}$-arch	2.6	2.8	26.7	99.2	213.7	1587.3

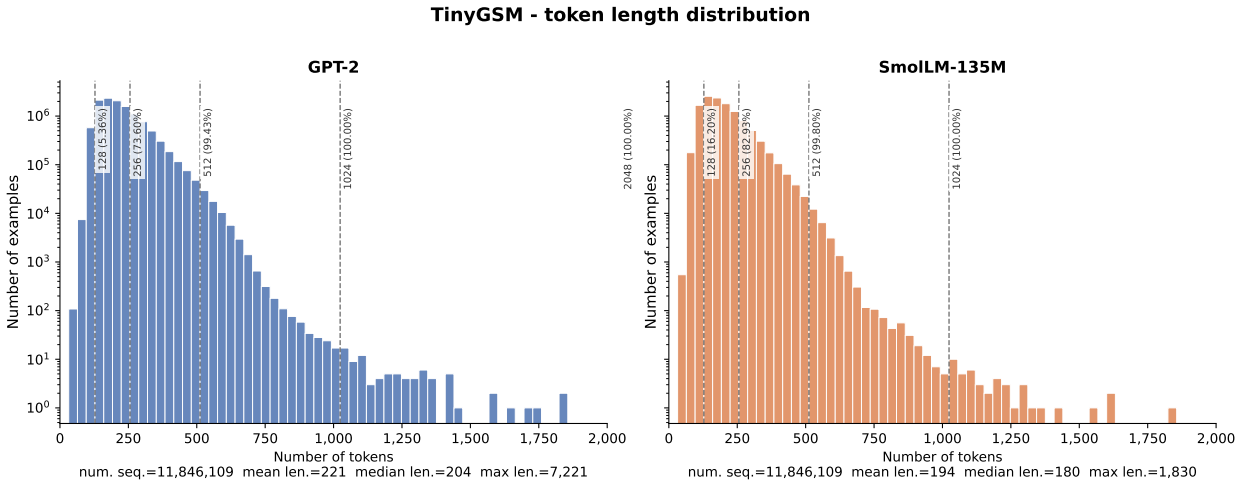

Figure 5: Distribution of tokenized sequence lengths on TinyGSM, under the GPT-2 tokenizer (left) and the `SmolLM-135M` tokenizer (right). The SmolLM tokenizer yields shorter sequences on average (median 204 vs. 180 tokens), which allows us to fit more problems in a fixed context length of 512 tokens.

C.2 Analysis under the Random Codebook Model

To derive (17), we use the standard concentration bound for inner products of uniform random vectors on the sphere (Vershynin, 2018, Theorem 3.4.5). For $\mathbf{X}, \mathbf{Y} \in \mathbb{S}^{d-1}$ with at least one of them sampled from $\mathcal{U}(\mathbb{S}^{d-1})$ and the other either fixed or independently sampled, for every $\epsilon > 0$:

$$\mathbb{P}\big(\mathbf{X}^\top \mathbf{Y} > \epsilon\big) \leq 2\exp\left(-\frac{d\epsilon^2}{2}\right). \tag{34}$$

The probability decreases exponentially in the dimension d.

Closed-form for the sampling dynamics Let $\mathbf{z}_\alpha = \mathrm{SLERP}(\mathbf{z}_0, \hat{\mathbf{e}}_k, \alpha)$ for $\alpha \in [0, 1]$. Then, by definition of SLERP, we have

$$\langle \mathbf{z}_\alpha, \hat{\mathbf{e}}_k \rangle = \cos\big(\omega(1-\alpha)\big), \tag{35}$$

where ω is the angle between $\mathbf{z}_0$ and $\hat{\mathbf{e}}_k$. Indeed, we recall the standard trigonometric identities

$$\sin(a-b) = \sin(a)\cos(b) - \cos(a)\sin(b) \tag{36}$$

and

$$\cos(a-b) = \cos(a)\cos(b) + \sin(a)\sin(b). \tag{37}$$

By the definition of SLERP in (8),

$$\mathbf{z}_\alpha = \frac{\sin((1-\alpha)\omega)}{\sin\omega}\,\mathbf{z}_0 + \frac{\sin(\alpha\omega)}{\sin\omega}\,\hat{\mathbf{e}}_k. \tag{38}$$

Therefore,

$$\begin{aligned}
\langle \mathbf{z}_\alpha, \hat{\mathbf{e}}_k\rangle &= \frac{\sin((1-\alpha)\omega)}{\sin\omega}\,\langle \mathbf{z}_0, \hat{\mathbf{e}}_k\rangle + \frac{\sin(\alpha\omega)}{\sin\omega} \\
&= \frac{1}{\sin\omega}\Big[\sin((1-\alpha)\omega)\cos\omega + \sin(\alpha\omega)\Big] \\
&= \frac{1}{\sin\omega}\Big[\big(\sin\omega\cos(\alpha\omega) - \cos\omega\sin(\alpha\omega)\big)\cos\omega + \sin(\alpha\omega)\Big] \\
&= \frac{1}{\sin\omega}\Big[\sin\omega\cos\omega\cos(\alpha\omega) - \cos^2\omega\sin(\alpha\omega) + \sin(\alpha\omega)\Big] \\
&= \frac{1}{\sin\omega}\Big[\sin\omega\cos\omega\cos(\alpha\omega) + (1-\cos^2\omega)\sin(\alpha\omega)\Big] \\
&= \frac{1}{\sin\omega}\Big[\sin\omega\cos\omega\cos(\alpha\omega) + \sin^2\omega\sin(\alpha\omega)\Big] \\
&= \cos\omega\cos(\alpha\omega) + \sin\omega\sin(\alpha\omega) \\
&= \cos(\omega - \alpha\omega) = \cos\big(\omega(1-\alpha)\big),
\end{aligned} \tag{39}$$

which proves (35). We can now derive (17).

Approximation 1 Since $\mathbf{z}_0$ and $\hat{\mathbf{e}}_k$ are independent random points on $\mathbb{S}^{d-1}$, (34) implies that they are close to orthogonal with high probability in high dimension. We therefore approximate the initial angle by

$$\omega \approx \frac{\pi}{2}. \tag{40}$$

Substituting this into (35) yields

$$\langle \mathbf{z}_\alpha, \hat{\mathbf{e}}_k\rangle \approx \cos\Big(\frac{\pi}{2}(1-\alpha)\Big) = \sin\Big(\frac{\pi}{2}\alpha\Big). \tag{41}$$

Approximation 2 Now define

$$M_\alpha := \max_{j\neq k}\langle \mathbf{z}_\alpha, \hat{\mathbf{e}}_j\rangle, \tag{42}$$

that is, the maximum similarity among codewords that the simplified generation dynamics does not interpolate toward. Using a union bound together with (34), we obtain

$$\mathbb{P}(M_\alpha \geq t \mid \mathbf{z}_\alpha) \leq \sum_{j\neq k}\mathbb{P}(\langle \mathbf{z}_\alpha, \hat{\mathbf{e}}_j\rangle > t \mid \mathbf{z}_\alpha) \leq 2(|\mathcal{V}|-1)\exp\left(-\frac{dt^2}{2}\right). \tag{43}$$

We now solve for the threshold $t_{|\mathcal{V}|,d,\delta}$ such that, with probability at least $1-\delta$, we have $M_\alpha < t_{|\mathcal{V}|,d,\delta}$. Concretely, we solve

$$\delta = 2(|\mathcal{V}|-1)\exp\left(-\frac{d\,t^2_{|\mathcal{V}|,d,\delta}}{2}\right), \tag{44}$$

which gives

$$t_{|\mathcal{V}|,d,\delta} = \sqrt{\frac{2\log\big(2(|\mathcal{V}|-1)/\delta\big)}{d}}. \tag{45}$$

Table 4: $\alpha^\star(\delta)$ for different $|\mathcal{V}|$, d, and δ.

$\lvert\mathcal{V}\rvert = 12$		
d	$\delta = 0.1$	$\delta = 0.01$
256	0.132	0.158
512	0.093	0.111
768	0.076	0.090
1024	0.065	0.078
4096	0.033	0.039

$\lvert\mathcal{V}\rvert = 50,000$		
d	$\delta = 0.1$	$\delta = 0.01$
256	0.213	0.231
512	0.149	0.161
768	0.121	0.131
1024	0.105	0.114
4096	0.052	0.057

$\lvert\mathcal{V}\rvert = 100,000$		
d	$\delta = 0.1$	$\delta = 0.01$
256	0.219	0.236
512	0.153	0.165
768	0.125	0.134
1024	0.108	0.116
4096	0.054	0.058

Table 5: Analytical noise schedules used on Sudoku, in the convention $\alpha_0 = 0$, $\alpha_1 = 1$.

Schedule	α_t
Linear	t
Cosine^2	$\sin^2\left(\frac{\pi t}{2}\right)$

We can now conclude by defining $\alpha^\star(\delta)$ as the interpolation level after which $\mathbf{z}_\alpha$ is most similar to $\hat{\mathbf{e}}_k$ with probability at least $1-\delta$. A sufficient condition is

$$\begin{aligned}
\cos\big((1-\alpha^\star)\omega\big) \approx \sin\Big(\frac{\pi}{2}\alpha^\star\Big) &\geq t_{|\mathcal{V}|,d,\delta} \\
\iff \sin\Big(\frac{\pi}{2}\alpha^\star\Big) &\geq \sqrt{\frac{2\log\big(2(|\mathcal{V}|-1)/\delta\big)}{d}} \\
\iff \alpha^\star(\delta) &\approx \frac{2}{\pi}\arcsin\left(\sqrt{\frac{2\log\big(2(|\mathcal{V}|-1)/\delta\big)}{d}}\right).
\end{aligned} \tag{46}$$

This concludes the argument.

Numerical evaluation of the critical threshold Table 4 shows the critical threshold for various vocabulary size $|\mathcal{V}|$, embedding dimension d, and confidence parameter δ. As expected, the threshold *decreases* as the embedding dimension increases, which means that the minimum noise level used during training should increase to counteract the increasing sparsity of $\mathbb{S}^{d-1}$. Furthermore, reducing δ corresponds to increasing the confidence level for similarity to the clean token being the largest, hence it means the minimal noise level is *smaller* than with a larger value of δ.

C.3 Sudoku Setup

We format the input as a 1D sequence, starting with the partial grid where the missing digits are encoded with `0`. We append a [BOS] separator and the solution, and separate rows with [SEP] . This representation allows us to train both AR and diffusion models with the same format with a context length of 180. Our vocabulary contains 12 tokens, except for MDLM, which additionally uses a [MASK] token. When training the diffusion models, the partial grid is never corrupted, and we never penalize the predictions on those positions.

We train all models with Adam for 20k steps, batch size 256, and a learning rate of 3×10^{-4} and an *Exponential Moving Average* (EMA) rate of 0.9999. For $\mathbb{S}$-FLM, we consider the linear and $\cos^2$ schedules and truncate following (17) (value in Table 4).

C.4 Additional Ablations on Sudoku

Table 6 ablates two design choices on Sudoku, the noise schedule and the embedding renormalization step. We define the noise schedules in Table 5.

Table 6: Effect of embedding renormalization on $\mathbb{S}$-FLM. Each row compares the same config without vs. with embedding re-normalization after every optimizer update. We **bold** the best result per row and difficulty. Training without re-normalization after each step leads to stronger performance.

	Without renorm			With renorm		
Schedule	Easy	Med.	Hard	Easy	Med.	Hard
Linear, no trunc	**81.5**	**50.6**	**14.0**	75.4	46.0	11.3
Linear, trunc $\alpha^\star(0.1)$	**94.0**	**77.6**	**43.2**	92.5	76.7	40.1
Cosine^2, no trunc	89.9	**68.0**	**36.1**	**92.1**	66.3	28.8
Cosine^2, trunc $\alpha^\star(0.1)$	**93.8**	**80.7**	**38.6**	92.9	76.4	34.1

Table 7: Effect of the truncation hyperparameter α_{trunc} on $\mathbb{S}$-FLM accuracy on GSM8K (trained on TinyGSM). Linear noise schedule, standard DiT backbone, 250k steps. The values 0.879 and 0.869 are the thresholds $\alpha^\star(\delta)$ from (17) at $\delta = 0.1$ and $\delta = 0.01$ respectively. **Bold** marks the best result.

α_{trunc}	Accuracy (%)
0.0	1.21
0.8	4.62
0.869	7.66
0.879	7.43
0.9	**7.73**

Effect of the noise schedule Truncating to $\alpha^\star(0.1)$ improves accuracy on both Sudoku (Table 1) and TinyGSM (Table 2). On Sudoku, the gains are largest for the linear schedule (Table 6). Cosine^2 also benefits from truncation, but by a smaller margin. Without truncation, Cosine^2 outperforms the linear schedule.

Effect of embedding renormalization Training without renormalizing the embeddings after each step improves accuracy across nearly all schedules and difficulties (Table 6). The gap is largest at the hard difficulty, reaching 7.3 points on Cosine^2 without truncation.

As discussed in Suppl. B.5, the gradient with respect to a normalized embedding is tangent to the sphere, so each gradient step increases the norm of the embeddings. This is equivalent to a learning-rate decay on the embedding table. Empirically, such annealing improves performance on Sudoku (Table 6).

C.5 Bootstrap Confidence Intervals on TinyGSM

The error bars on the TinyGSM accuracy plots are 95% percentile bootstrap confidence intervals (Efron, 1979; Raschka, 2022). The GSM8K test split contains $N = 1{,}319$ problems, each with a generated solution that is either correct or incorrect. We resample the N outcomes with replacement $B = 1{,}000$ times and recompute the accuracy on every resample. The point estimate is the mean of the B accuracies. The error bar runs from the 2.5% quantile of the B resample accuracies to the 97.5% quantile, namely the 2.5th and 97.5th percentiles of the empirical bootstrap accuracy distribution.

C.6 Additional Ablations on TinyGSM

Table 7 sweeps the truncation hyperparameter α_{trunc} on the linear schedule, with the standard DiT backbone trained for 250k steps. Truncating the noise schedule improves the accuracy from 1.21% at $\alpha_{\text{trunc}} = 0$ to 7.73% at $\alpha_{\text{trunc}} = 0.9$. The thresholds from (17) for $d = 768$ and $|\mathcal{V}| \approx 50$k, $\alpha^\star(0.1) = 0.879$ and $\alpha^\star(0.01) = 0.869$, perform similarly to the best run ($\alpha_{\text{trunc}} = 0.9$).

C.7 Additional Sampling Results on TinyGSM

For models trained on TinyGSM, we sweep architecture, sampling temperature, and velocity decoding, and report GSM8K accuracy. Figure 6 replots Figure 1 (right). At $T = 0.1$, Duo reaches 36.0% and MDLM about 33%, while $\mathbb{S}$-FLM plateaus near 18%. Figure 7 compares the $\mathbb{S}$-arch and standard DiT backbones at both temperatures, with $T = 0.1$ improving GSM8K accuracy by about six points for both. Figure 8 sweeps the top-k truncation of velocity decoding for $\mathbb{S}$-arch at $T = 1$. Top-1 reaches 18.0%, while $k \geq 10$ plateau near 12%, matching unrestricted decoding.

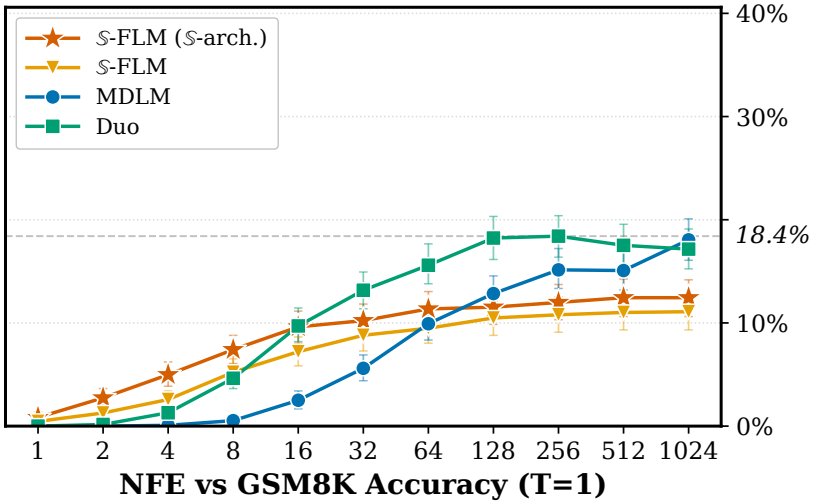

Figure 6: GSM8K accuracy vs. NFE at $T = 1$ for 𝕊-FLM (𝕊-arch and standard DiT), MDLM, and Duo. Same data as Figure 1 (right).

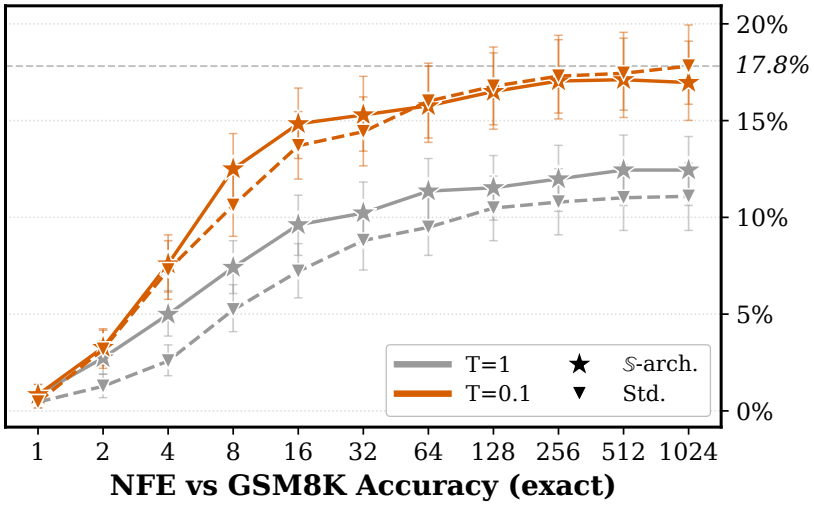

Figure 7: GSM8K accuracy vs. NFE under exact decoding for 𝕊-FLM with 𝕊-arch (Norm.) and standard DiT (Std.), at $T = 1$ (grey) and $T = 0.1$ (orange). Lowering the temperature improves accuracy by about six points for both backbones.

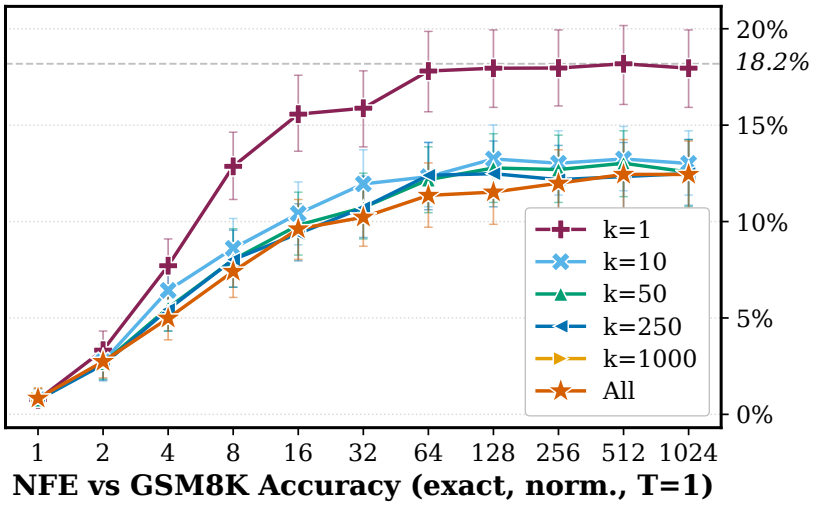

Figure 8: GSM8K accuracy vs. NFE for $\mathbb{S}$-FLM ($\mathbb{S}$-arch) at $T = 1$, sweeping the top-k truncation of the predicted velocity field at each Euler step. Top-1 reaches 18.0%, while $k \geq 10$ all plateau near 12%, matching unrestricted decoding.

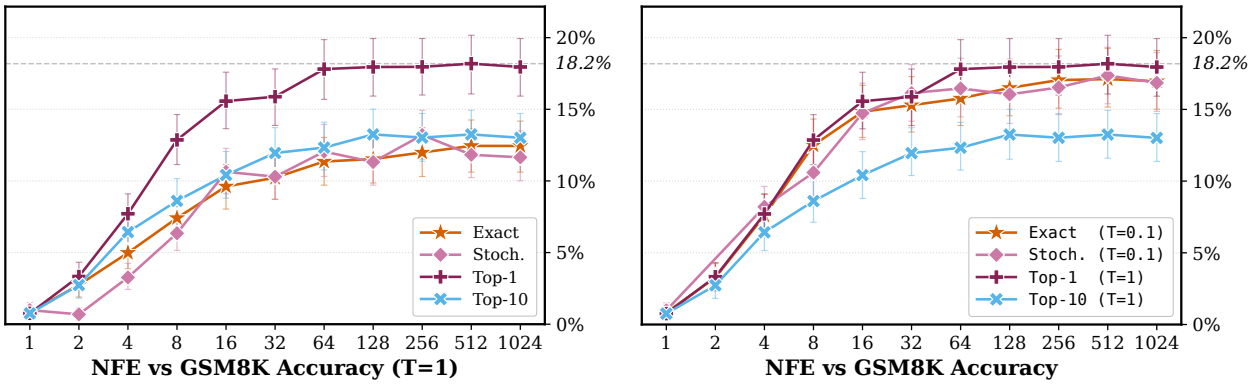

Figure 9: GSM8K accuracy vs. NFE for $\mathbb{S}$-FLM ($\mathbb{S}$-arch) under exact velocity, stochastic, top-1, and top-10 decoding. **(left)** Sampling temperature $T = 1$. Exact velocity and stochastic decoding plateau near 12%, while top-1 reaches 18.0%. **(right)** Sampling temperature $T = 0.1$. All four schemes plateau within one point of 18.0%. Top-1 decoding ($T = 1$) outperforms low-temperature stochastic decoding.

C.8 Gen. PPL / Entropy Frontier Protocol

We adopt the same setup as in PGM (Deschenaux et al., 2025). For each method (MDLM, Duo, FLM, and $\mathbb{S}$-FLM with exact, stochastic, and $k = 1$ velocity decoding), we sweep the sampling temperature $T \in \{0.50, 0.55, \ldots, 1.20\}$ (15 evenly-spaced values) and the number of function evaluations $\text{NFE} \in \{32, 64, 128, 256, 512, 1024\}$. For every (T, NFE) cell, we draw $N = 512$ samples of length $L = 1024$ from the OpenWebText-trained model and compute two scalars per sample.

Generative Perplexity We score each generated sample with a pretrained GPT-2-large reference model (Deschenaux et al., 2025) and report the per-sample average

$$\text{PPL}_{\text{gen}} = \exp\left(-\frac{1}{L}\sum_{i=1}^{L} \log p_{\text{GPT2}}(x_i \mid x_{<i})\right), \tag{47}$$

masking tokens at or after the first end-of-text. We average across the N samples in the cell.

Unigram entropy To flag degenerate (repetitive) outputs, we compute the per-cell mean unigram entropy (Deschenaux et al., 2025)

$$H = -\frac{1}{N}\sum_{n=1}^{N}\sum_{v\in\mathcal{V}}\frac{c(v,x^{(n)})}{L}\log\frac{c(v,x^{(n)})}{L}, \tag{48}$$

where $c(v, x^{(n)})$ counts the occurrences of token v in sample $x^{(n)}$.

Visible window Each cell contributes one $(H, \mathrm{PPL}_{\mathrm{gen}})$ point. We restrict the visible window to $4.5 \leq H \leq 6.0$ nats and $\mathrm{PPL}_{\mathrm{gen}} \leq 500$ to drop collapsed and degenerate configurations. $\mathbb{S}$-FLM with $k = 1$ velocity does not depend on the temperature, so it appears as a single marker rather than a curve.

C.9 Additional Results on OpenWebText

Figure 10 shows the Gen. PPL / Entropy front for NFEs $\in \{32, 64, 128, 256, 512, 1024\}$.

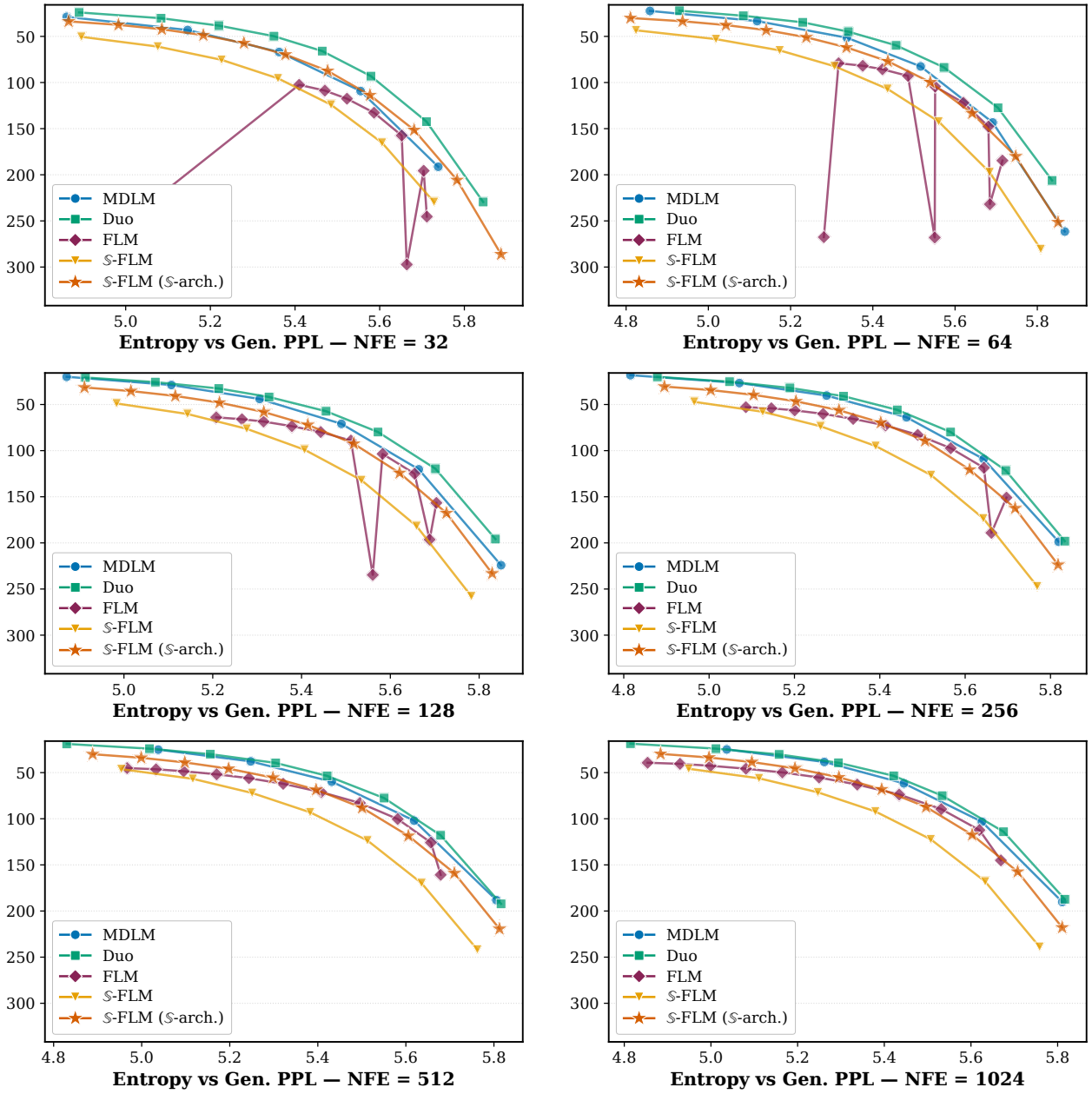

Figure 10: OpenWebText Gen. PPL versus per-sample unigram entropy for NFE $\in \{32, 64, 128, 256, 512, 1024\}$. Each curve sweeps a sampling-temperature schedule. $\mathbb{S}$-FLM (exact velocity and stochastic decoding) traces the Pareto frontier across every NFE budget, with the largest margin over MDLM, Duo, and FLM at low NFE.

D Extended Related Work

$\mathbb{S}$-FLM differs from prior work in three main ways. (1) It operates in continuous rather than discrete space, (2) defines the flow on the hypersphere rather than in Euclidean space, and (3) learns embeddings end-to-end instead of relying on pre-trained representations.

Discrete diffusion language models Discrete diffusion models for text (Austin et al., 2023; Campbell et al., 2022; Lou et al., 2024; Sahoo et al., 2024; Gat et al., 2024; Campbell et al., 2024; Sahoo et al.,

2025a; Deschenaux et al., 2026; Shi et al., 2025; Nie et al., 2025; Sahoo et al., 2025b; von Rütte et al., 2025; Deschenaux et al., 2025; von Rütte et al., 2026; Sahoo et al., 2026; Arriola et al., 2025) approach AR in Gen. PPL while enabling parallel generation, but require updating tokens independently at inference for tractability. Furthermore, because the sampling steps are not differentiable, gradient-based guidance (Dhariwal & Nichol, 2021; Ho & Salimans, 2022; Nisonoff et al., 2024; Schiff et al., 2025) is harder than in the continuous case.

Continuous diffusion for language modeling Instead of operating in the discrete space of tokens, certain prior work use Gaussian diffusion (Sohl-Dickstein et al., 2015; Ho et al., 2020) for language modeling. One approach is to apply Gaussian diffusion to embeddings and train end-to-end with CE (Li et al., 2022; Dieleman et al., 2022; Gulrajani & Hashimoto, 2023). Alternatively, others regress onto pre-trained embeddings (Strudel et al., 2022; Lovelace et al., 2022; Shen et al., 2026). The latter requires two training stages, and the sample quality is capped by the pre-trained embeddings. Instead of embeddings, recent work add Gaussian noise to one-hot or simplex representations of the tokens (Chen et al., 2022; Han et al., 2023; Mahabadi et al., 2023; Stark et al., 2024; Lee et al., 2026; Roos et al., 2026; Potaptchik et al., 2026). This approach requires storing dense arrays $L \times |\mathcal{V}|$ during training and sampling. Separately, Loopholing discrete diffusion (Jo et al., 2025) allows discrete diffusion models to propagate the latent representation of the denoiser across sampling steps. $\mathbb{S}$-FLM is defined on the latent hypersphere. Therefore, it does not require the materialization of dense arrays $L \times |\mathcal{V}|$ during training. We inject noise by rotating embeddings rather than adding Gaussian noise.

Representation learning on the hypersphere Hyperspherical representations are common in contrastive learning, where uniform spread in $\mathbb{S}^{d-1}$ correlates with strong downstream performance (Wang & Isola, 2020). Comparing word embeddings with cosine similarity performs better than using the Euclidean distance in high dimension (Mikolov et al., 2013; Pennington et al., 2014). Thus, cosine similarity underpins a large part of neural retrieval systems (Reimers & Gurevych, 2019; Karpukhin et al., 2020). Training Variational Autoencoders with a latent prior in $\mathbb{S}^{d-1}$ can be more stable than with Gaussian priors (Davidson et al., 2018; Xu & Durrett, 2018). Normalizing activations and weights to $\mathbb{S}^{d-1}$ can also improve the stability of AR models (Loshchilov et al., 2024). In Riemannian manifolds, predicting the clean endpoint can outperform regressing the velocity field (Eijkelboom et al., 2025; Zaghen et al., 2026). Previous work extended CNFs and score-based diffusion to Riemannian Manifolds (Lou et al., 2020; Mathieu & Nickel, 2020; Bortoli et al., 2022; Lou et al., 2023). However, they typically assume data already reside on the manifold. In contrast, we learn the token representation and the velocity on $\mathbb{S}^{d-1}$ jointly. Fisher-Flow (Davis et al., 2024) maps one-hot vector on the positive orthant of the hypersphere, but this representation does not perform well on language modeling with large vocabularies (Jo & Hwang, 2025).